AN ABSTRACT OF THE THESIS OF

Siddharth Suhaschandra Chandgadkar for the degree of Master of Science in Mechanical Engineering presented on May 22, 2001. Title: Performance of a Smart Direct Fire Penetrator using a Ram Air Controlled Mechanism.

Redacted for privacy

Abstract approved: _____

Mark F.Costello

The effectiveness of a direct fire penetrator projectile equipped with an actively controlled ram air mechanism is investigated through dynamic simulation. The ram air control mechanism consists of a rotary sleeve valve which directs air flow from an inlet at the center of the nose to side ports. The projectile dynamics, the inertial measurement unit and the control system are included in the system model. It is shown that the ram air control mechanism provides sufficient control authority to significantly reduce dispersion of a direct fire penetrator. The effects of accelerometer and gyroscope bias and noise are investigated. It is seen that moderate values of bias and noise do not affect the dispersion significantly. But with higher values the dispersion is greater than the dispersion for the free flight.

Performance of a Smart Direct Fire Penetrator using a Ram Air Controlled Mechanism

by

Siddharth Suhaschandra Chandgadkar

A THESIS

Submitted to

Oregon State University

in partial fulfillment of
the requirements for the
degree of

Master of Science

Completed May 22, 2001
Commenced June 2002

Master of Science of Siddharth Suhaschandra Chandgadkar presented on May 22, 2001

APPROVED:

Redacted for privacy

Major Professor, representing Mechanical Engineering

Redacted for privacy

Chair of Department of Mechanical Engineering

Redacted for privacy

Dean of Graduate School

I understand that my thesis will become part of the permanent collection of Oregon State University libraries. My signature below authorizes release of my thesis to any reader upon request.

Redacted for privacy

Siddharth Suhaschandra Chandgadkar, Author

ACKNOWLEDGEMENT

I would like to thank Dr. Mark F.Costello for his patience and guidance and for the many hours he spent with me on this work. I would also like to thank Dr. Deborah V.Pence and Dr. James A.Liburdy for their guidance. Finally, I would like to thank my Father, Mother and Sister for their support and their unending belief in me.

TABLE OF CONTENTS

LIST OF FIGURES

LIST OF FIGURES, CONTINUED

LIST OF TABLES

LIST OF SYMBOLS

x, y, z : Position vector components of the projectile mass center expressed in the inertial reference frame.

ϕ, θ, ψ : Euler roll, pitch, and yaw angles of the projectile.

u, v, w : Translation velocity components of the projectile mass center resolved in the body reference frame.

p, q, r : Components of the projectile angular velocity vector expressed in the body reference frame.

$\tilde{x}, \tilde{y}, \tilde{z}$: Estimated position vector components of the projectile mass center in the inertial reference frame.

$\tilde{\phi}, \tilde{\theta}, \tilde{\psi}$: Estimated projectile Euler roll, pitch, and yaw angles.

$\tilde{u}, \tilde{v}, \tilde{w}$: Estimated translation velocity components of the IMU resolved in the body reference frame.

$\tilde{p}, \tilde{q}, \tilde{r}$: Estimated components of the projectile angular velocity vector expressed in the body reference frame.

$\tilde{a}_X, \tilde{a}_Y, \tilde{a}_Z$: Estimated components of the IMU acceleration vector expressed in the body reference frame.

X, Y, Z : Total external force components on the projectile expressed in the body reference frame.

LIST OF SYMBOLS, CONTINUED

X_W, Y_W, Z_W : Weight components of the projectile expressed in the body reference frame.

X_A, Y_A, Z_A : Standard aerodynamic force components on the projectile expressed in the body reference frame.

X_R, Y_R, Z_R : Ram air force components expressed in the body reference frame.

L, M, N : Total external moment components on the projectile expressed in the body reference frame.

m : Free flight projectile mass.

I : Mass moment of inertia matrix.

D : Projectile characteristic length.

C_i : Projectile aerodynamic coefficients.

α : Longitudinal aerodynamic angle of attack.

β : Lateral aerodynamic angle of attack.

Δ : Stationline distance from the projectile base to mass center.

g : Gravitational constant.

p_s : Pressure at the conical surface.

p_i : Pressure at location i.

ρ_i : Density at location i.

T_i : Temperature at location i.

LIST OF SYMBOLS, CONTINUED

V_i : Velocity at location i.

Ma_i : Mach number at location i.

f : Friction factor for the ram air cavities.

L_c : Length of one ram air cavity.

γ : Ratio of specific heats.

D_c : Diameter of the ram air cavities.

γ_y, γ_z : Pseudo controls.

$e_i, \dot{e}_i, e_{ii}$: Error, error derivative, integral error for the i^{th} coordinate.

k_{di}, k_{pi}, k_{ii} : Derivative gain, proportional gain, integral gain for the i^{th} coordinate.

Performance of a Smart Direct Fire Penetrator using a Ram Air Controlled Mechanism

1. INTRODUCTION

Maneuvering projectiles offers the potential for significant improvements in gun system ammunition through improved hit probability. Increasing concerns over collateral damage, environmental damage, and efficiency of military operations have all heightened the need to substantially increase the accuracy of future weapon systems. Depending on specific mission requirements, maneuvering projectiles offers the ability to extend the range at which a target can be engaged, improves weapon accuracy, corrects for initial aiming errors and target maneuvers, reduces time to kill, and provides off-boresight target kill capability. However, successful application of control technology to medium and small caliber munitions presents two significant technological challenges, namely, development of miniature sensor suites with associated sensor processing and the development of simple and small control mechanisms. These devices must not only be small but must also be capable of surviving the launch environment.

Many projectile control mechanisms have been conceived. These concepts generally fall into one of two categories: aerodynamic control or jet thrust control. Examples of aerodynamic controls include: deflecting tail fins, canard lifting surfaces, deflecting nose tips, spoilers, and ram air deflection controls. Examples of jet thrust controls include: warm gas jet thrusters, impulse thrusters, and

explosive thrusters. For low muzzle velocity systems, where dynamic pressure is relatively low, jet thruster systems offer large control authority. However, as dynamic pressure increases, aerodynamic control offers the potential for higher control authority. An aerodynamic control mechanism that is particularly attractive for high velocity direct fire weapons is the ram air control mechanism pictured in Figure 1. The ram air control mechanism is a simple system. Mounted at the front end of the projectile is a rotary sleeve valve which directs ram air from the central inlet in the nose through exit ports on the sides of the nose. By properly angling the ports, sufficient thrust is developed while reducing the drag penalty of the inlet. Dynamic control moments are achieved by rotating the sleeve valve so that maximum output flow is from the port which is opposite to the direction of the commanded side force. The control valve is the only moving part within the control mechanism and it has a low mass moment of inertia and aerodynamic torque. Furthermore, significant control forces are immediately available at launch due to the high launch velocity of penetrator type projectiles. Moreover, the nose area is available "real estate", as the nose section consists only of a wind screen since a blunt penetrator improves target impact performance.

While the ram air control concept offers great potential for future smart weapon systems, little research has been undertaken regarding this control concept. White, Hempling, Prodan, and Conboy[1] performed the first studies on a guided, gun launched ram air projectile. Their study focused on the feasibility of a helicopter launched projectile in the 25-40mm caliber range to correct for a 3

milliradian aiming error and a 3g maneuver of the target. Two exit nozzles directed flow from the inlet port. The ram air control mechanism had three states, namely, equal flow through both exit ports, flow through exit port 1, and flow through exit port 2.

The work reported here seeks to expand the literature base on this type of control mechanism applied to a smart penetrator projectile. With this in mind, an integrated simulation including coupled dynamics of the projectile body and the sensor suite which contains an Inertial Measurement Unit (IMU) is exercised to examine the performance of an examplar configuration. A trajectory tracking controller using feedback linearization forms the flight control system. For the example configuration, dispersion caused by initial projectile angular rate perturbations is shown for the uncontrolled and controlled cases. Parametric studies on the effect of ram air inlet diameter size, IMU accelerometer bias, IMU gyroscope bias, IMU accelerometer noise, and IMU gyroscope noise on projectile dispersion are reported.

2. DYNAMIC MODELLING

2.1 REFERENCE FRAMES

To model the dynamics of the projectile two reference frames are used. These are shown in Figure 1. The inertial reference frame is a stationary frame. It is located at the exit of the of the gun muzzle. The body frame is a mobile frame that is attached to the projectile with its origin at the center of gravity of the round. This frame rotates and translates with respect to the inertial frame. The $\vec{I}_B$ axis is aligned with the axis of symmetry of the projectile. The $\vec{J}_B$ and the $\vec{K}_B$ axis form a right handed triple.

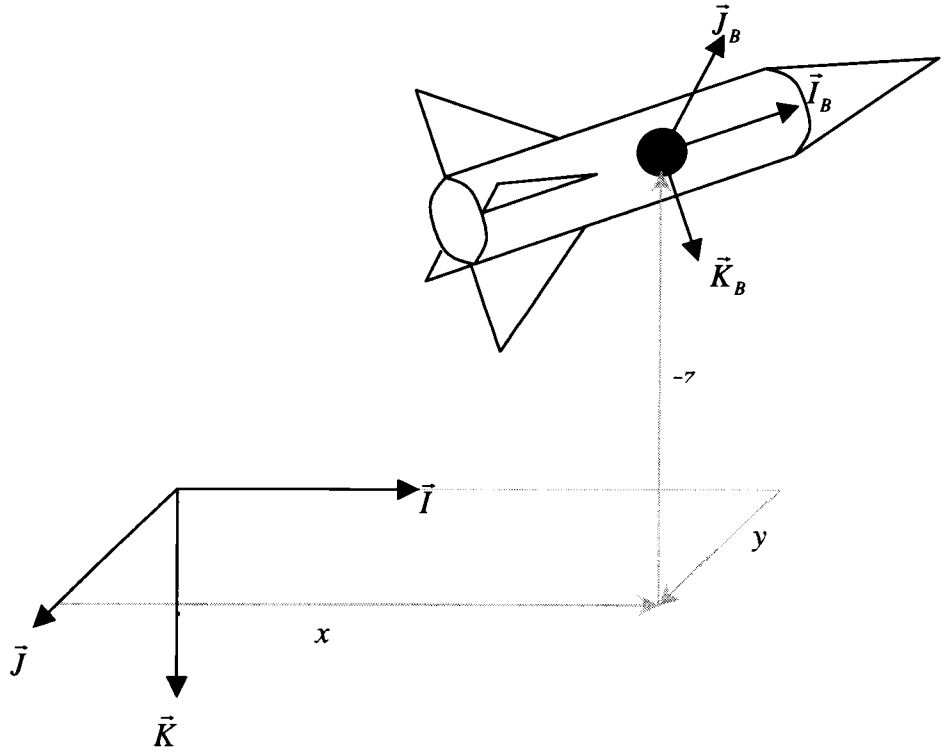

Figure 1. Reference frames and body position coordinates.

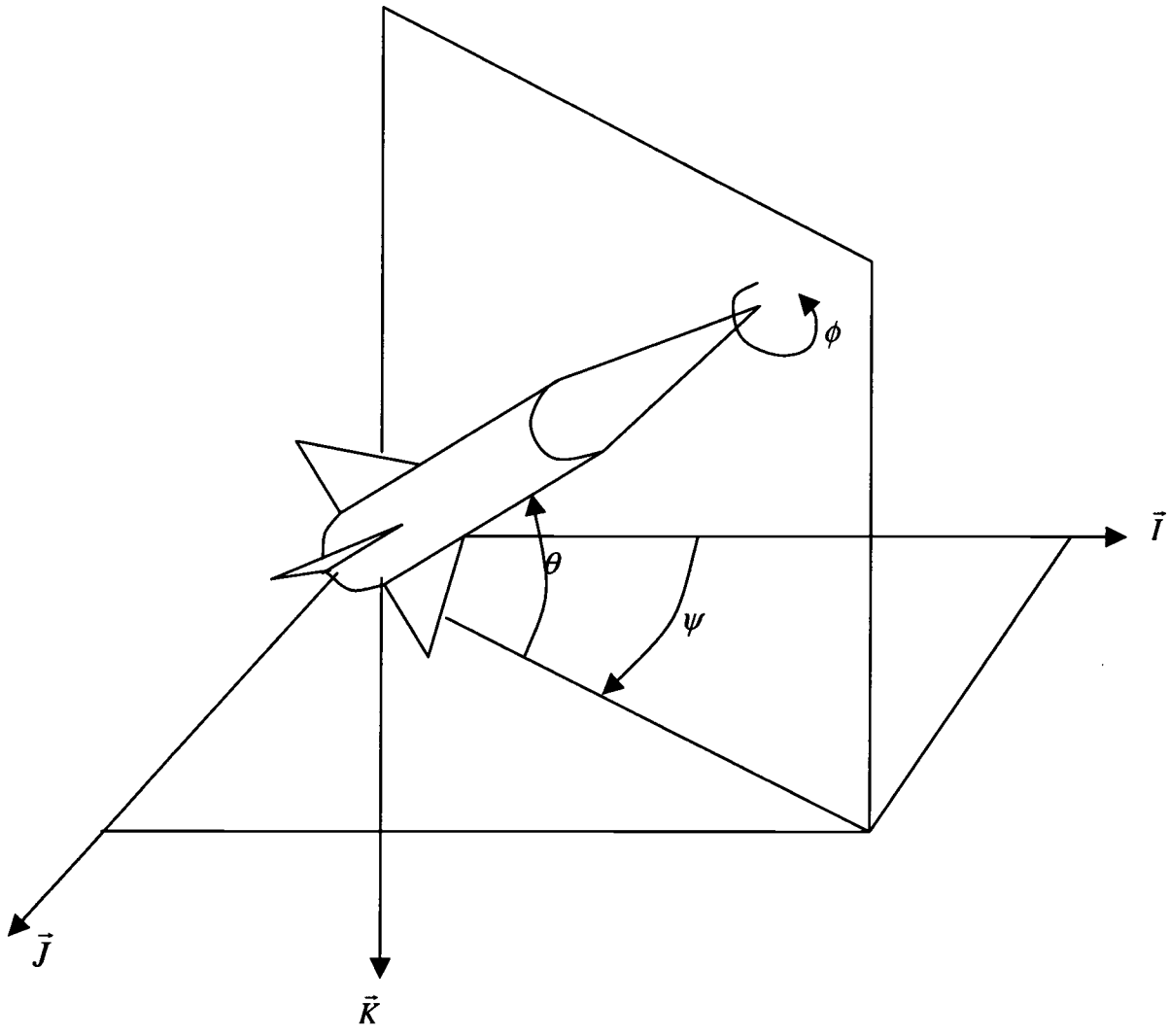

Figure 2. Projectile angular orientation.

The round has six degrees of freedom, of which three are translational and three are rotational. The translational degrees of freedom are the body position coordinates x, y, z as shown in Figure 1. The rotational degrees of freedom are the Euler angles ψ, θ, ϕ as shown in Figure 2. The yaw, pitch and roll angles are

denoted as ψ, θ and ϕ respectively. These are defined according to the standard convention for Euler angles[11].

2.2 DYNAMIC EQUATIONS

The dynamic equations are written with respect to the body frame. The projectile translational and rotational kinematic and dynamic equations[2,11] are given by equations (1) to (4).

$$\begin{Bmatrix} \dot{x} \\ \dot{y} \\ \dot{z} \end{Bmatrix} = [T] \begin{Bmatrix} u \\ v \\ w \end{Bmatrix} \tag{1}$$

$$\begin{Bmatrix} \dot{\phi} \\ \dot{\theta} \\ \dot{\psi} \end{Bmatrix} = \begin{bmatrix} 1 & \sin\phi\tan\theta & \cos\phi\tan\theta \\ 0 & \cos\phi & -\sin\phi \\ 0 & \sin\phi/\cos\theta & \cos\phi/\cos\theta \end{bmatrix} \begin{Bmatrix} p \\ q \\ r \end{Bmatrix} \tag{2}$$

$$\begin{Bmatrix} \dot{u} \\ \dot{v} \\ \dot{w} \end{Bmatrix} = \begin{Bmatrix} X/m \\ Y/m \\ Z/m \end{Bmatrix} - \begin{bmatrix} 0 & -r & q \\ r & 0 & -p \\ -q & p & 0 \end{bmatrix} \begin{Bmatrix} u \\ v \\ w \end{Bmatrix} \tag{3}$$

$$\begin{Bmatrix} \dot{p} \\ \dot{q} \\ \dot{r} \end{Bmatrix} = [I]^{-1} \left[\begin{Bmatrix} L \\ M \\ N \end{Bmatrix} - \begin{bmatrix} 0 & -r & q \\ r & 0 & -p \\ -q & p & 0 \end{bmatrix} [I] \begin{Bmatrix} p \\ q \\ r \end{Bmatrix} \right] \tag{4}$$

where,

$$T=\begin{bmatrix}\cos\theta\cos\psi & \sin\phi\sin\theta\cos\psi-\cos\phi\sin\psi & \cos\phi\sin\theta\cos\psi+\sin\phi\sin\psi\\ \cos\theta\sin\psi & \sin\phi\sin\theta\sin\psi+\cos\phi\cos\psi & \cos\phi\sin\theta\sin\psi-\sin\phi\cos\psi\\ -\sin\theta & \sin\phi\cos\theta & \cos\phi\cos\theta\end{bmatrix} \quad (5)$$

$$I=\begin{bmatrix}I_{XX} & I_{XY} & I_{XZ}\\ I_{XY} & I_{YY} & I_{YZ}\\ I_{XZ} & I_{YZ} & I_{ZZ}\end{bmatrix} \quad (6)$$

T is the body to inertial frame rotation transformation matrix. This is a composite product of 3 body fixed rotations corresponding to the Euler angles outlined previously. The inertia matrix is denoted by I. The round that is being used for this study is symmetric so that the products of inertia for this configuration are zero.

The total force components X,Y,Z acting on the projectile consist of contributions from the weight of the round($_W$), the standard aerodynamic forces($_A$) and the ram air control forces($_R$) as given by equation (7)

$$\begin{Bmatrix}X\\ Y\\ Z\end{Bmatrix}=\begin{Bmatrix}X_W\\ Y_W\\ Z_W\end{Bmatrix}+\begin{Bmatrix}X_A\\ Y_A\\ Z_A\end{Bmatrix}+\begin{Bmatrix}X_R\\ Y_R\\ Z_R\end{Bmatrix} \quad (7)$$

The weight portion of the total loads is given by equation (8),

$$\begin{Bmatrix}X_W\\ Y_W\\ Z_W\end{Bmatrix}=mg\begin{Bmatrix}-\sin\theta\\ \sin\phi\cos\theta\\ \cos\phi\cos\theta\end{Bmatrix} \quad (8)$$

The standard aerodynamic force contribution is given by equations (9) through (11).

$$\begin{Bmatrix} X_A \\ Y_A \\ Z_A \end{Bmatrix} = -q_a \begin{Bmatrix} C_{X0} + C_{X2}(\alpha^2 + \beta^2) \\ C_{y0} + C_{NA}\beta \\ C_{z0} + C_{NA}\alpha \end{Bmatrix} \tag{9}$$

$$\alpha = \tan^{-1}\left(\frac{w}{u}\right) \qquad \beta = \tan^{-1}\left(\frac{v}{u}\right) \tag{10}$$

$$q_a = \frac{1}{8}\rho(u^2 + v^2 + w^2)\pi D^2 \tag{11}$$

The ram air force is a function of the Mach number, the angle of attack and the ram air cavity configuration. In this study, only its dependence on the Mach number is considered. This can be justified by the fact the variation in angle of attack is small. The maximum values of lateral forces generated by the ram air mechanism for any given diameter are calculated for several values of free stream Mach numbers and then linearly interpolated during simulation. The details of these calculations are given in Chapter 5.

The external moments result from the steady ($_{SA}$) and unsteady ($_{UA}$) body aerodynamics and the ram air force ($_{R}$) as given by equation (12).

$$\begin{Bmatrix} L \\ M \\ N \end{Bmatrix} = \begin{Bmatrix} L_{SA} \\ M_{SA} \\ N_{SA} \end{Bmatrix} + \begin{Bmatrix} L_{UA} \\ M_{UA} \\ N_{UA} \end{Bmatrix} + \begin{Bmatrix} L_R \\ M_R \\ N_R \end{Bmatrix} \tag{12}$$

The steady state aerodynamic moments are computed from a cross product between the distance vector from the mass center of the projectile to the center of pressure and the steady aerodynamic body force above and are given by equation (13). The center of pressure location is dependent on local Mach number and is computed by linear interpolation.

$$\begin{Bmatrix} L_{SA} \\ M_{SA} \\ N_{SA} \end{Bmatrix} = -q_a \begin{bmatrix} 0 & -Z_{cop} & Y_{cop} \\ Z_{cop} & 0 & -X_{cop} \\ -Y_{cop} & X_{cop} & 0 \end{bmatrix} \begin{Bmatrix} C_{X0} + C_{X2}(\alpha^2 + \beta^2) \\ C_{Y0} + C_{NA}\beta \\ C_{Z0} + C_{NA}\alpha \end{Bmatrix} \tag{13}$$

The unsteady body aerodynamic moment provides a damping source for projectile angular motion and is given by equations (14).

$$\begin{Bmatrix} L_{UA} \\ M_{UA} \\ N_{UA} \end{Bmatrix} = q_a D \begin{Bmatrix} C_{DD} + \dfrac{pDC_{LP}}{2V} \\ \dfrac{qDC_{MQ}}{2V} \\ \dfrac{rDC_{NR}}{2V} \end{Bmatrix} \tag{14}$$

The ram air forces are assumed to act at the exit of the ram air cavities. The ram air moments can be then computed as a cross product between the radius vector from the mass center to the ram air cavity exit and the lateral ram air forces. The above dynamic model has been correlated with free flight range data for a typical penetrator configuration and agreement between the model and measured data is good[2]. The maximum error between the predicted states and measured states is 0.01%.

3. FLIGHT CONTROL SYSTEM

3.1 INTRODUCTION

The equations of motion are highly non-linear. The usual practice of designing a controller at several trim points and then using gain scheduling to achieve tracking, results in degraded performance at dynamic states away from the trim points. A more efficient control technique is needed for the present case. Non-linear control manifests itself as a solution to the present problem.

Of the several non-linear control techniques available, feedback linearization is used for the present study. The advantage of this technique is its simplicity and ease of application. The implementation of feeback linearization scheme is shown in Figure 3. This technique involves relating the states to be

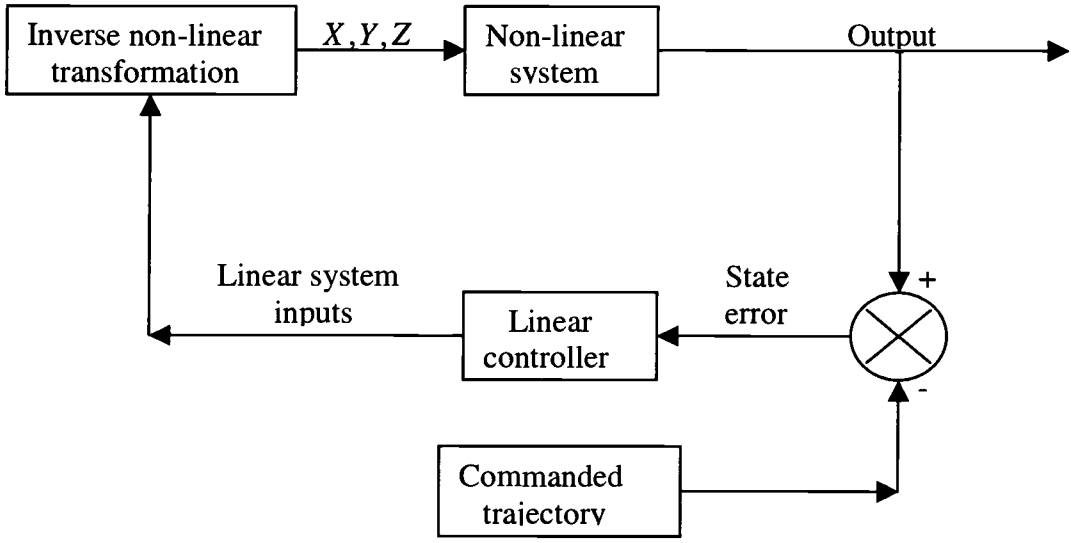

Figure 3. Feedback Linearization scheme.

controlled to the inputs and then linearizing the system using pseudo controls. A controller is then designed in the linear domain to meet tracking specifications. The input to the actual non-linear system is calculated by transforming the input to the linear system via the inverse non-linear transformation into the actual inputs *X,Y,Z.*

3.2 FLIGHT CONTROL SYSTEM DYNAMIC MODEL

Though the ram air control mechanism generates 3 force components, only 2 are used to control altitude (z) and cross range (y) of the projectile.

The body position coordinates x, y, z are taken to be the outputs of the system, with y, z being the controlled outputs. The inputs to the system are the total applied loads on the body along the $\vec{J}_B$ axis and the $\vec{K}_B$ axis, namely, Y and Z. The dynamic equation for the system outputs, i.e, equation (1), is not related to the system inputs. To relate the system inputs to the outputs, equation (1) is differentiated. The result is equation(15).

$$\begin{Bmatrix} \ddot{x} \\ \ddot{y} \\ \ddot{z} \end{Bmatrix} = \frac{1}{m} \begin{bmatrix} T_{11} & T_{12} \\ T_{21} & T_{22} \end{bmatrix} \begin{Bmatrix} X \\ Y \\ Z \end{Bmatrix} \tag{15}$$

where, $T_{11}, T_{12}, T_{21}, T_{22}$ are sub-matrices formed from the body to inertial rotation transformation matrix T. T_{11} is a scalar, T_{12} is a 1×2 row vector, T_{21} is 2×1 column vector and T_{22} is a 2×2 matrix. The matrix equation (15) relates the two

inertial body position coordinates y, z to the force components Y, Z as given by equation (16).

$$\begin{Bmatrix} \ddot{y} \\ \ddot{z} \end{Bmatrix} = \frac{1}{m}[T_{21}]\{X\} + \frac{1}{m}[T_{22}]\begin{Bmatrix} Y \\ Z \end{Bmatrix} \tag{16}$$

In equation (16), the body force component X contains terms from the aerodynamic force and the weight force. The forces Y, Z represent the total force that should act on the round in the body frame to achieve the required lateral tracking. The right hand side of equation (16) is treated as a pseudo control vector γ which results in a linear system of the form given by equation (17).

$$\begin{Bmatrix} \ddot{y} \\ \ddot{z} \end{Bmatrix} = \begin{Bmatrix} \gamma_y \\ \gamma_z \end{Bmatrix} \tag{17}$$

The pseudo controls, γ_y and γ_z, are designed in the linear domain to achieve the required tracking performance. The actual forces Y and Z are obtained by transforming the output of the linear system via the inverse non-linear transformation into the real coordinates as given by equation (18).

$$\begin{Bmatrix} Y \\ Z \end{Bmatrix} = [T_{22}]^{-1}\left(m\begin{Bmatrix} \gamma_y \\ \gamma_z \end{Bmatrix} - [T_{21}]\{X\} \right) \tag{18}$$

The force components Y, Z in equation (18) represent the total commanded force or the net force that should act on the round. Apart from the ram air force, the total force also has contributions from the steady state aerodynamic force and the weight. These are subtracted from the result of equation (18) to obtain the commanded ram air control force as given by equation (19).

$$\begin{Bmatrix} Y_R \\ Z_R \end{Bmatrix} = \begin{Bmatrix} Y \\ Z \end{Bmatrix} - \begin{Bmatrix} Y_A \\ Z_A \end{Bmatrix} - \begin{Bmatrix} Y_W \\ Z_W \end{Bmatrix} \tag{19}$$

3.3 LINEAR DESIGN

A proportional, integral, and derivative (PID) controller is used in the present study. When properly tuned a PID controller can provide suitable tracking performance. Use of feedback requires knowledge of the integral of tracking error, which in turn generates two additional state equations in the flight control system. These are given by equation (20) to (21).

$$\dot{e}_{iy} = e_y \tag{20}$$

$$\dot{e}_{iz} = e_z \tag{21}$$

With the values of the errors e_y, e_z, error derivatives $\dot{e}_y, \dot{e}_z$ and error integrals e_{iy}, e_{iz} known, the PID control law used in the feedback path for the linear equivalent is given by equation (22) to (23).

$$\gamma_y = -k_{py} e_y - k_{dy} \dot{e}_y - k_{iy} e_{iy} \tag{22}$$

$$\gamma_z = -k_{pz} e_z - k_{dz} \dot{e}_z - k_{iz} e_{iz} \tag{23}$$

To achieve effective tracking, the dynamics of this controller have to be as fast as the projectile dynamics. A controller slower than the projectile will result in a sluggish operation of the ram air control mechanism. On the other hand, a very fast controller will lead to error attenuation. The maximum force that can be generated by the ram air mechanism at any Mach number also places limitations on the controller gains. The proportional gain k_{pi}, derivative gain k_{di} and integral gain k_{ii} are chosen such that satisfactory tracking is achieved in the linear domain. These controller gains are tuned further in the non-linear domain to achieve the required sensitivity and to accommodate for the maximum force limit due to the ram air mechanism. With these factors in consideration and the use of standard linear design techniques the gains evaluated for use in this study are $k_{pi} = 50.0$, $k_{di} = 2.0$ and $k_{ii} = 54.6$. The initial gains are calculated using pole placement and further tuned in the non-linear domain to get the optimal performance. Figure 4 and Figure 5 show the tracking performance of the linear system for the altitude and the cross range with these gains.

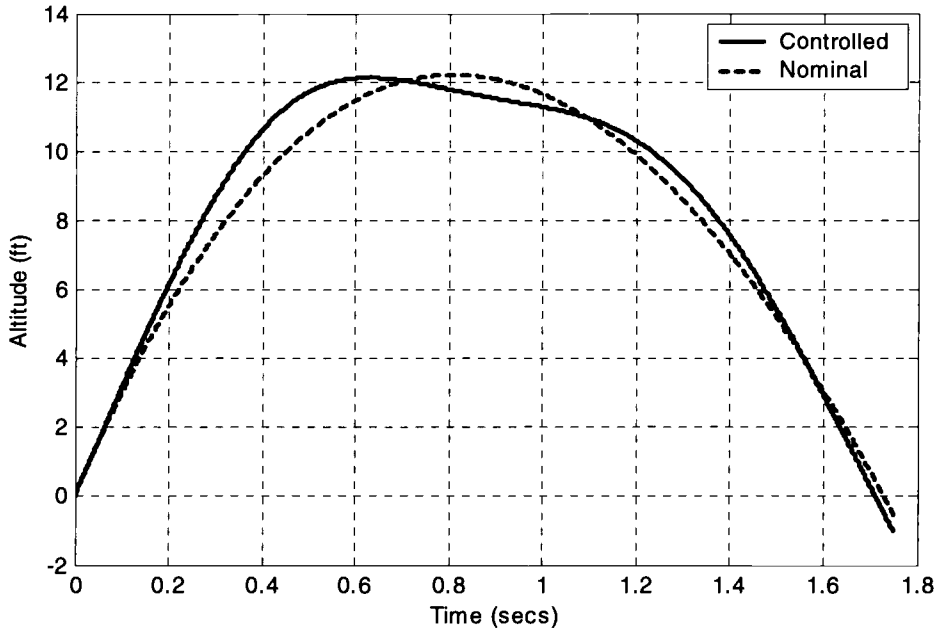

Figure 4. Altitude tracking for the linear system.

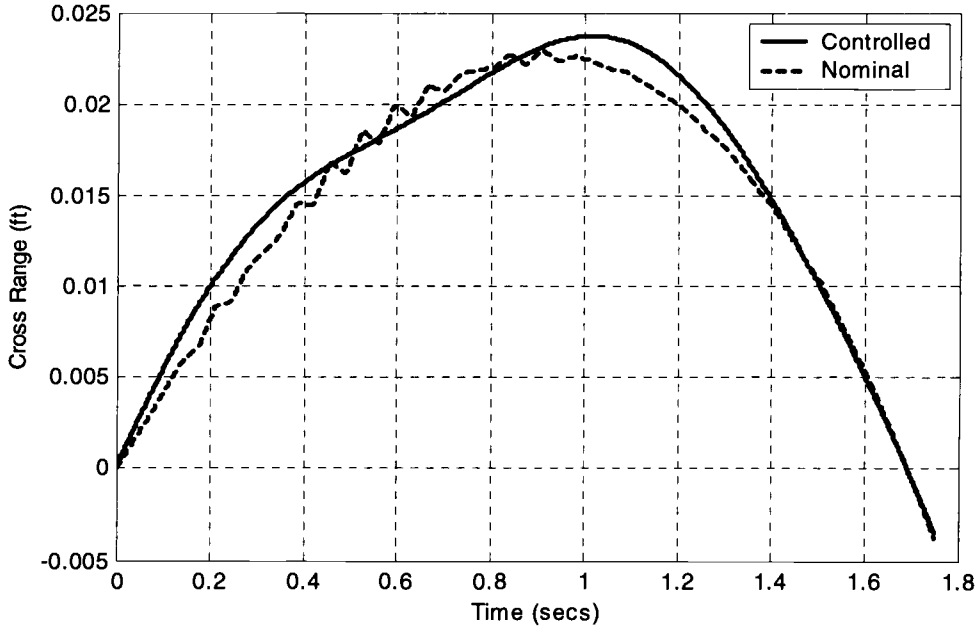

Figure 5. Cross Range tracking for the linear system.

4. INERTIAL MEASUREMENT UNIT

4.1 DYNAMIC EQUATIONS

To achieve feedback linearization, state measurement and feedback is needed. An Inertial Measurement Unit (IMU) exactly serves this purpose[14]. It uses measured angular velocity and linear acceleration of the round and subsequently utilizes this sensor input to estimate the full state of the projectile. Consider an IMU as shown in Figure 6.

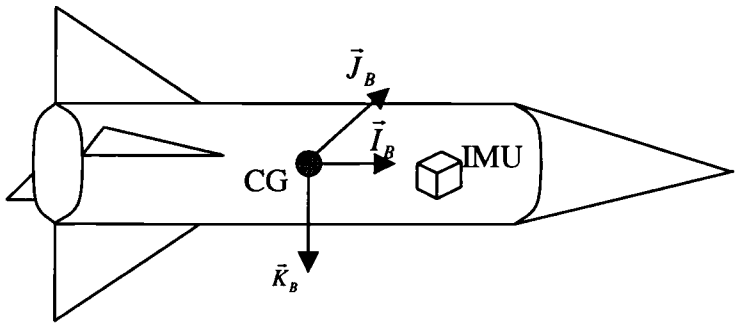

Figure 6. Inertial Measurement Unit.

It consists of a set of 3 uni-axially sensitive gyroscopes and 3 uni-axially sensitive accelerometers. These are mounted in the IMU in such a manner that the sensitive axes of the IMU are aligned to the body reference frame. The acceleration as recorded by the IMU is denoted by $\tilde{a}_X\vec{I}_B + \tilde{a}_Y\vec{J}_B + \tilde{a}_Z\vec{K}_B$ and the angular velocity by $\tilde{p}\vec{I}_B + \tilde{q}\vec{J}_B + \tilde{r}\vec{K}_B$. The differential equations for the IMU estimated CG location are given by equation (24).

$$\begin{Bmatrix} \dot{\tilde{x}} \\ \dot{\tilde{y}} \\ \dot{\tilde{z}} \end{Bmatrix} = \left[\tilde{T}\right]\left(\begin{Bmatrix} \tilde{u} \\ \tilde{v} \\ \tilde{w} \end{Bmatrix} - \begin{bmatrix} 0 & -\tilde{r} & \tilde{q} \\ \tilde{r} & 0 & -\tilde{p} \\ -\tilde{q} & \tilde{p} & 0 \end{bmatrix} \begin{Bmatrix} x_{CG\to IMU} \\ y_{CG\to IMU} \\ z_{CG\to IMU} \end{Bmatrix} \right) \tag{24}$$

The kinematic differential equations for the Euler angles of the IMU are given by equation (25).

$$\begin{Bmatrix} \dot{\tilde{\phi}} \\ \dot{\tilde{\theta}} \\ \dot{\tilde{\psi}} \end{Bmatrix} = \begin{bmatrix} 1 & \sin\tilde{\phi}\tan\tilde{\theta} & \cos\tilde{\phi}\tan\tilde{\theta} \\ 0 & \cos\tilde{\phi} & -\sin\tilde{\phi} \\ 0 & \sin\tilde{\phi}/\cos\tilde{\theta} & \cos\tilde{\phi}/\cos\tilde{\theta} \end{bmatrix} \begin{Bmatrix} \tilde{p} \\ \tilde{q} \\ \tilde{r} \end{Bmatrix} \tag{25}$$

The differential equations for the velocity of the IMU are given by equation (26).

$$\begin{Bmatrix} \dot{\tilde{u}} \\ \dot{\tilde{v}} \\ \dot{\tilde{w}} \end{Bmatrix} = \begin{Bmatrix} \tilde{a}_X \\ \tilde{a}_Y \\ \tilde{a}_Z \end{Bmatrix} - \begin{bmatrix} 0 & -\tilde{r} & \tilde{q} \\ \tilde{r} & 0 & -\tilde{p} \\ -\tilde{q} & \tilde{p} & 0 \end{bmatrix} \begin{Bmatrix} \tilde{u} \\ \tilde{v} \\ \tilde{w} \end{Bmatrix} \tag{26}$$

The acceleration at the IMU is given by equation (27).

$$\begin{Bmatrix} a_X^* \\ a_Y^* \\ a_Z^* \end{Bmatrix} = \begin{Bmatrix} \dot{u} \\ \dot{v} \\ \dot{w} \end{Bmatrix} + \begin{bmatrix} 0 & -r & q \\ r & 0 & -p \\ -q & p & 0 \end{bmatrix} \begin{Bmatrix} u \\ v \\ w \end{Bmatrix} + \begin{bmatrix} -q^2 - r^2 & pq - \dot{r} & pr + \dot{q} \\ pq + \dot{r} & -p^2 - r^2 & qr - \dot{p} \\ pr - \dot{q} & qr + \dot{p} & -p^2 - q^2 \end{bmatrix} \begin{Bmatrix} x_{CG \to IMU} \\ y_{CG \to IMU} \\ z_{CG \to IMU} \end{Bmatrix} \tag{27}$$

The accelerometers measure gravitational acceleration in addition to the projectile acceleration. The net acceleration as recorded by the accelerometer is given by equation (28).

$$\begin{Bmatrix} a_{XT}^* \\ a_{YT}^* \\ a_{ZT}^* \end{Bmatrix} = \begin{Bmatrix} a_X^* \\ a_Y^* \\ a_Z^* \end{Bmatrix} + \begin{Bmatrix} -g\sin\theta \\ g\cos\theta\sin\phi \\ g\cos\theta\cos\phi \end{Bmatrix} \tag{28}$$

4.2 MODEL OF THE SENSOR ERROR

The IMU is prone to sensor errors, which manifest themselves as noise and bias in the accelerometer and the gyroscope readings. These have a great impact on the performance of the flight control system as IMU provides the flight control system with values of position coordinates derived from the sensed accelerometer and gyroscope readings. To evaluate the extent to which the performance of the flight control system is affected by the sensor error, it needs to be modeled. This section addresses this issue.

As stated previously, the IMU consists of a set of 3 uni-axially sensitive accelerometers and 3 uni-axially sensitive gyroscopes with their sensitive axis aligned with the body frame axes. The sensor frame is chosen such that the x axis of the sensor frame is aligned with the sensitive sensor axis. The transformation matrices from the body frame to the sensor frame are denoted by T_{S1}^{g}, T_{S2}^{g} and T_{S3}^{g} for the gyroscopes and by T_{S1}^{a}, T_{S2}^{a} and T_{S3}^{a} for the accelerometers respectively.

The readings of the accelerometers and the gyroscopes are corrupted with noise. The sensors also have an inherent bias associated with them. Noise usually introduces a Gaussian deviation from the actual value. The bias represents a constant difference between the actual state and the sensed reading. Both of these entities mislead the controller by falsifying the current location reading supplied to the flight control system.

To simulate the actual readings of the accelerometers and the gyroscopes, noise and bias are added to the actual acceleration readings from equation (28) and to the actual angular velocity of the round to get the corrupted readings, recorded by the IMU. These corrupted readings are given by equations (29) to (30).

$$\begin{Bmatrix} a_{1XS} \\ a_{2XS} \\ a_{3XS} \end{Bmatrix} = \begin{Bmatrix} a_{1N} + a_{1B} \\ a_{2N} + a_{2B} \\ a_{3N} + a_{3B} \end{Bmatrix} + \left[T_{sense}^{a} + T_{CAY}^{a} + T_{CAZ}^{a} \right] \begin{Bmatrix} a_{XT}^{*} \\ a_{YT}^{*} \\ a_{ZT}^{*} \end{Bmatrix} \tag{29}$$

$$\begin{Bmatrix} \omega_{1XS} \\ \omega_{2XS} \\ \omega_{3XS} \end{Bmatrix} = \begin{Bmatrix} \omega_{1N} + \omega_{1B} \\ \omega_{2N} + \omega_{2B} \\ \omega_{3N} + \omega_{3B} \end{Bmatrix} + \left[T^{g}_{sense} + T^{g}_{CAY} + T^{g}_{CAZ} \right] \begin{Bmatrix} p \\ q \\ r \end{Bmatrix} \tag{30}$$

where,

$$T^{a}_{sense} = \begin{bmatrix} T^{a}_{S1}(1,1) & T^{a}_{S1}(1,2) & T^{a}_{S1}(1,3) \\ T^{a}_{S2}(1,1) & T^{a}_{S2}(1,2) & T^{a}_{S2}(1,3) \\ T^{a}_{S3}(1,1) & T^{a}_{S3}(1,2) & T^{a}_{S3}(1,3) \end{bmatrix} \tag{31}$$

$$T^{a}_{CAY} = \begin{bmatrix} T^{a}_{S1}(1,1)C^{a}_{1Y} & T^{a}_{S1}(1,2)C^{a}_{1Y} & T^{a}_{S1}(1,3)C^{a}_{1Y} \\ T^{a}_{S2}(1,1)C^{a}_{2Y} & T^{a}_{S2}(1,2)C^{a}_{2Y} & T^{a}_{S2}(1,3)C^{a}_{2Y} \\ T^{a}_{S3}(1,1)C^{a}_{3Y} & T^{a}_{S3}(1,2)C^{a}_{3Y} & T^{a}_{S3}(1,3)C^{a}_{3Y} \end{bmatrix} \tag{32}$$

$$T^{a}_{CAZ} = \begin{bmatrix} T^{a}_{S1}(1,1)C^{a}_{1Z} & T^{a}_{S1}(1,2)C^{a}_{1Z} & T^{a}_{S1}(1,3)C^{a}_{1Z} \\ T^{a}_{S2}(1,1)C^{a}_{2Z} & T^{a}_{S2}(1,2)C^{a}_{2Z} & T^{a}_{S2}(1,3)C^{a}_{2Z} \\ T^{a}_{S3}(1,1)C^{a}_{3Z} & T^{a}_{S3}(1,2)C^{a}_{3Z} & T^{a}_{S3}(1,3)C^{a}_{3Z} \end{bmatrix} \tag{33}$$

$$T^{g}_{sense} = \begin{bmatrix} T^{g}_{S1}(1,1) & T^{g}_{S1}(1,2) & T^{g}_{S1}(1,3) \\ T^{g}_{S2}(1,1) & T^{g}_{S2}(1,2) & T^{g}_{S2}(1,3) \\ T^{g}_{S3}(1,1) & T^{g}_{S3}(1,2) & T^{g}_{S3}(1,3) \end{bmatrix} \tag{34}$$

$$T^{g}_{CAY} = \begin{bmatrix} T^{g}_{S1}(1,1)C^{g}_{1Y} & T^{g}_{S1}(1,2)C^{g}_{1Y} & T^{g}_{S1}(1,3)C^{g}_{1Y} \\ T^{g}_{S2}(1,1)C^{g}_{2Y} & T^{g}_{S2}(1,2)C^{g}_{2Y} & T^{g}_{S2}(1,3)C^{g}_{2Y} \\ T^{g}_{S3}(1,1)C^{g}_{3Y} & T^{g}_{S3}(1,2)C^{g}_{3Y} & T^{g}_{S3}(1,3)C^{g}_{3Y} \end{bmatrix} \tag{35}$$

$$T^{g}_{CAZ} = \begin{bmatrix} T^{g}_{S1}(1,1)C^{g}_{1Z} & T^{g}_{S1}(1,2)C^{g}_{1Z} & T^{g}_{S1}(1,3)C^{g}_{1Z} \\ T^{g}_{S2}(1,1)C^{g}_{2Z} & T^{g}_{S2}(1,2)C^{g}_{2Z} & T^{g}_{S2}(1,3)C^{g}_{2Z} \\ T^{g}_{S3}(1,1)C^{g}_{3Z} & T^{g}_{S3}(1,2)C^{g}_{3Z} & T^{g}_{S3}(1,3)C^{g}_{3Z} \end{bmatrix} \tag{36}$$

The sensors are prone to cross axis sensitivity, which means that angular velocities from axes perpendicular to the sensitive axis constitute a small percentage of the sensor readings. This can be very detrimental, especially in the case of a system where the angular velocities in one channel are very large. For example, consider a sensor used for a spin stabilized projectile with a roll rate of 5000 rad/s and a pitch rate of 1 rad/s. A cross axis sensitivity of just one percent, implies that the pitch rate read by the gyroscope will be 51 rad/s instead of the actual 1 rad/s and this may lead to disaster. The matrices T^{a}_{CAY}, T^{a}_{CAZ} in equations (32) to (33) and T^{g}_{CAY}, T^{g}_{CAZ} in equations (35) to (36) model this effect.

Usually an estimate of bias is available from the manufacturer of the sensor. But noise cannot be estimated. Thus the reading of the IMU can be corrected by subtracting out the manufacturer supplied bias. In fact, by using two different values of bias – the actual value and the manufacturer estimated value, the effect of the discrepancy in the bias value can be evaluated. The resulting linear accelerations at the IMU and body angular velocities as recorded by the IMU are used in the state equations for the IMU and are given by equations (37) to (38).

$$\begin{Bmatrix} \tilde{a}_X \\ \tilde{a}_Y \\ \tilde{a}_Z \end{Bmatrix} = \left[T^a_{sense} + T^a_{CAY} + T^a_{CAZ} \right]^{-1} \begin{Bmatrix} a_{1XS} - a_{1B} \\ a_{2XS} - a_{2B} \\ a_{3XS} - a_{3B} \end{Bmatrix} - \begin{Bmatrix} -gs_\theta \\ gc_\theta s_\phi \\ gc_\theta c_\phi \end{Bmatrix} \tag{37}$$

$$\begin{Bmatrix} \tilde{p} \\ \tilde{q} \\ \tilde{r} \end{Bmatrix} = \left[T^g_{sense} + T^g_{CAY} + T^g_{CAZ} \right]^{-1} \begin{Bmatrix} \omega_{1XS} - \omega_{1B} \\ \omega_{2XS} - \omega_{2B} \\ \omega_{3XS} - \omega_{3B} \end{Bmatrix} \tag{38}$$

5. RAM AIR MECHANISM

5.1 DESCRIPTION

The ram air mechanism consists of a cavity at the tip of the nose of the round, which divides into a number of side cavities inside the conical nose. Together these are called as the ram air cavities. The side cavities are inclined to the $\vec{I}_B$ axis of the projectile and open on the surface of the conical nose as shown in Figure 7.

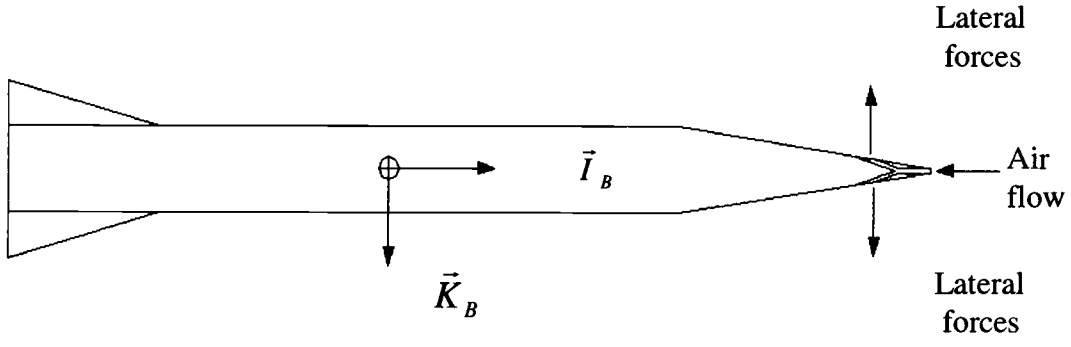

Figure 7. The concept of ram air mechanism.

In this study, the number of side cavities is equal to four. Air flowing into the central inlet is ducted to side cavities and during this process of momentum change, a force is imparted to the walls of the side cavities. The magnitude of this force is a direct function of the projectile velocity. If the flow of air through the

cavity is altered, the force imparted to the round is also altered. This is achieved by placing a rotary sleeve valve in the each of the side cavities. The sleeve valve is a device which acts like a variable diameter orifice. By changing the diameter of the valve, the flow through the side cavities is changed.

5.2 RAM AIR FORCES

In the present work, a control volume approach is used to determine the lateral force generated due to air flow in a single ram air duct as shown in Figure 8.

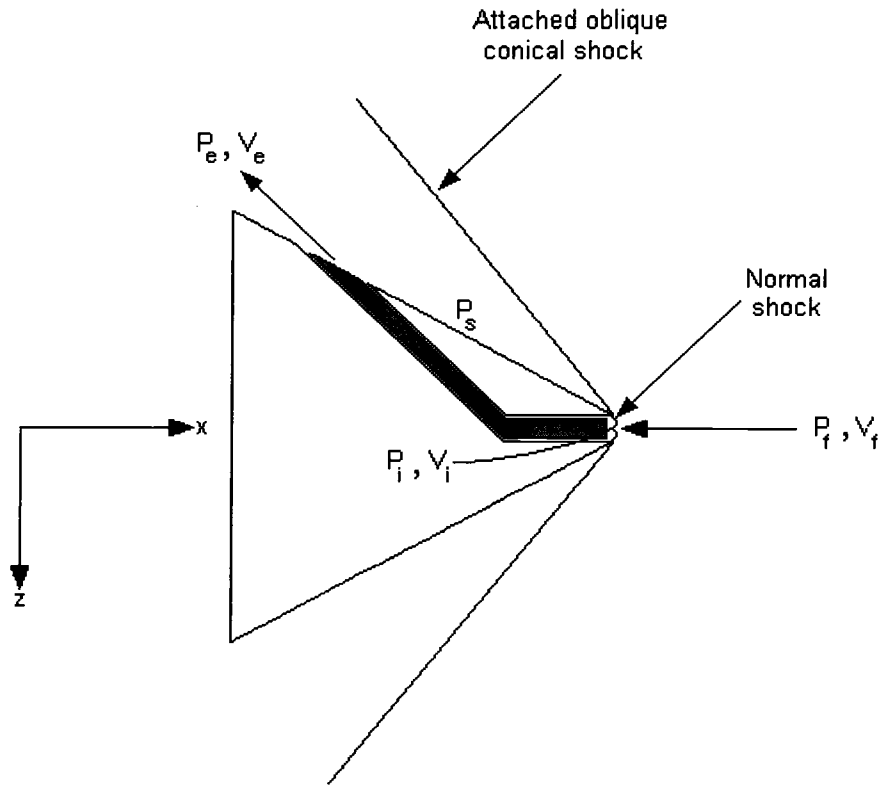

Figure 8 – Flow through one ram air cavitiy in the projectile nose.

A normal shock is assumed at the ram air cavity entrance and an attached conical shock is assumed around the nose of the projectile. The characteristics of the flow are calculated by using ideal gas relationships across a normal shock for the ram intake and oblique shock relationships for the external flow. The flow inside the duct is assumed to be adiabatic with friction. The friction factor is calculated from Moody's relationships[12] assuming a smooth walled tube. It is also assumed that the internal flow is not affected by the duct curvature. The pressure on the surface of the cone downstream of the oblique shock is calculated by the use of surface pressure coefficient SPC [13] which is defined by equation (39).

$$SPC = \frac{p_s - p_f}{\frac{1}{2}\rho_f V_f^2} \tag{39}$$

The subscripts s and f refer to the surface and the free stream properties respectively. The ram flow velocity at the duct exit is determined from the local Mach number Ma_e within the ram cavity. This Mach number is the solution to the flow with friction[12] given by equation (40).

$$\frac{fL_c}{D_c} = \frac{\gamma+1}{2\gamma}\ln\left[\frac{1+\frac{(\gamma-1)}{2}Ma_e^2}{1+\frac{(\gamma-1)}{2}Ma_i^2}\right] - \frac{1}{\gamma}\left[\frac{1}{Ma_e^2} - \frac{1}{Ma_i^2}\right] - \frac{\gamma+1}{2\gamma}\ln\left[\frac{Ma_e^2}{Ma_i^2}\right] \tag{40}$$

The subscripts i and e refer to the inlet and the exit of the ram air cavity respectively. With the Mach number at the exit known, equations (41) to (43) below are used to evaluate the flow properties at the exit[12].

$$\frac{p_e}{p_i} = \frac{Ma_i}{Ma_e}\left[\frac{1+\frac{(\gamma-1)}{2}Ma_i^2}{1+\frac{(\gamma-1)}{2}Ma_e^2}\right]^{1/2} \tag{41}$$

$$\frac{\rho_e}{\rho_i} = \frac{Ma_i}{Ma_e}\left[\frac{1+\frac{(\gamma-1)}{2}Ma_e^2}{1+\frac{(\gamma-1)}{2}Ma_i^2}\right]^{1/2} \tag{42}$$

$$\frac{T_e}{T_i} = \frac{1+\frac{(\gamma-1)}{2}Ma_i^2}{1+\frac{(\gamma-1)}{2}Ma_e^2} \tag{43}$$

Once the flow conditions are determined, a momentum balance through the duct is used to determine the lateral force acting on the projectile as given by equation (44).

$$Z_{R\max} = -\dot{m}V_{out,z} + (PA)_{out,z} \tag{44}$$

5.3 RAM AIR FORCE TABLES

Table 1 shows the ram air forces calculated for different orifice diameters at various inlet Mach numbers using the relations listed in the previous section.

		ORIFICE DIAMETER (mm)						
MACH NUMBER		*3*	*2.7*	*2.4*	*2.1*	*1.8*	*1.5*	*1.2*
	5	10.4516	8.5103	6.7594	5.2109	3.8678	2.7224	1.7801
	4.5	8.8276	7.1749	5.7075	4.3993	3.2646	2.3008	1.5060
	4	7.3496	5.9702	4.7582	3.6728	2.7289	1.9253	1.2631
	3.5	6.0593	4.9392	3.9271	3.0348	2.2572	1.5961	1.0519
	3	4.9597	4.0427	3.2212	2.4878	1.8541	1.3167	0.8729
	2.5	4.0323	3.2925	2.6291	2.0446	1.5292	1.0940	0.7358
	2	3.3358	2.7385	2.2020	1.7223	1.3131	0.9699	0.7907

Table 1. Maximum lateral ram air control forces (lbf).

The inlet Mach number changes during flight. To accommodate this change, the lateral forces calculated above are linearly interpolated during simulation. At any one time only two cavities remain active. This is due to the way in which the cavities are located with respect to the body reference frame. Each of the side cavities is situated in a plane of the body frame. Thus, a force commanded in the y direction of the body frame requires either one of the two cavities located in the $\vec{I}_B - \vec{J}_B$ plane to remain active.

6. RESULTS

The first thing to verify was the performance of the controller. To this end, a nominal trajectory was generated by perturbing the initial conditions of the round. The aim was to generate a trajectory with a hit point at $(0,0)$ in a plane parallel to the inertial y, z plane at two kilometers down range.

Total weight of projectile (lbf)	6.9883
Stationline of center of gravity, *slcg* (ft)	0.6505
Buttline of center of gravity (ft), *blcg*	0.0000
Waterline of center of gravity (ft), *wlcg*	0.0000
Moment of inertia (slug-ft^2), I_{XX}	0.00065873
Moment of inertia (slug-ft^2), I_{YY}	0.03347783
Moment of inertia (slug-ft^2), I_{ZZ}	0.03347783
Moment of inertia (slug-ft^2), I_{XY}	0.0000
Moment of inertia (slug-ft^2), I_{XZ}	0.0000
Moment of inertia (slug-ft^2), I_{YZ}	0.0000
Reference diameter for aero coefficients (ft), D	0.12434

Table 2. Round properties.

Table 2 lists the round properties and Table 3 lists the initial values used for the nominal trajectory generation.

Initial x inertial position (ft)	0.0000
Initial y inertial position (ft)	0.0000
Initial z inertial position (ft)	0.0000
Initial yaw angle (rad), ψ	-0.000069
Initial pitch angle (rad), θ	0.00515
Initial bank angle (rad), ϕ	0.0000
Initial forward velocity (ft/s), u	5589.12
Initial side velocity (ft/s), v	0.4428
Initial vertical velocity (ft/s), w	-2.99464
Initial roll rate (r/s), p	10.0000
Initial pitch rate (r/s), q	1.06
Initial yaw rate (r/s), r	-0.0135

Table 3. Nominal initial simulation values.

To test the controller, the nominal initial values for the pitch and the yaw rates were perturbed. The results of this perturbation are shown from Figure 9 to Figure 31.

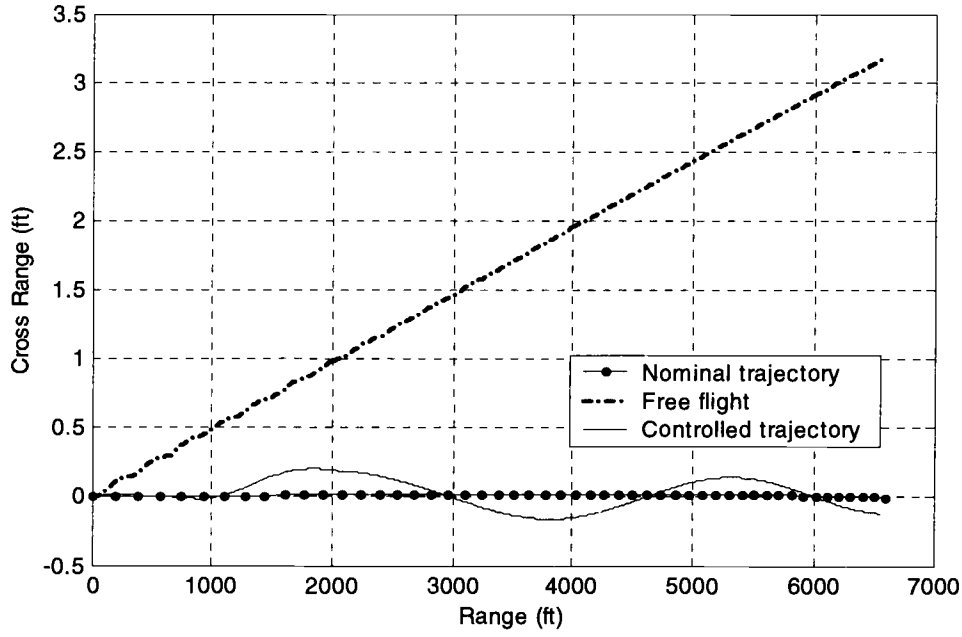

Figure 9. Cross range vs Range.

Figure 9 shows the performance of the controller cross range tracking. The nominal cross range is almost a horizontal line. The controlled range is seen to fluctuate, but the deviation from the nominal trajectory is small (about 0.2 feet maximum).

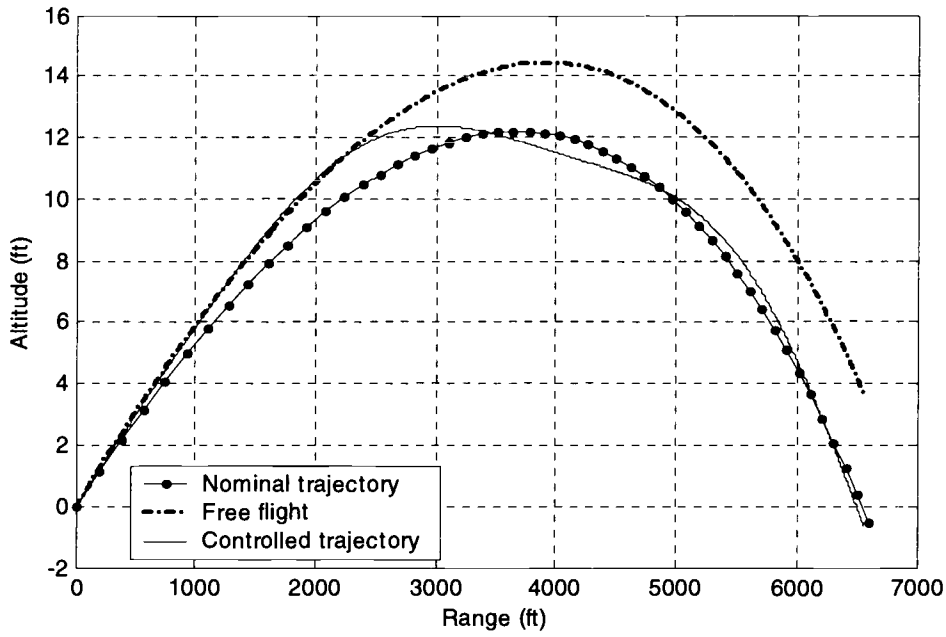

Figure 10. Altitude vs Range.

Figure 10 shows the performance of the controller altitude tracking. The response of the controller at the beginning is sluggish and not much control activity is seen. This is due to the values of the controller gains. To improve the initial response, the controller gains could be increased. But this would result in high control forces which cannot be generated by the ram air mechanism. The controller starts to respond at about 2000 feet down range and from then on smoothly tracks the altitude.

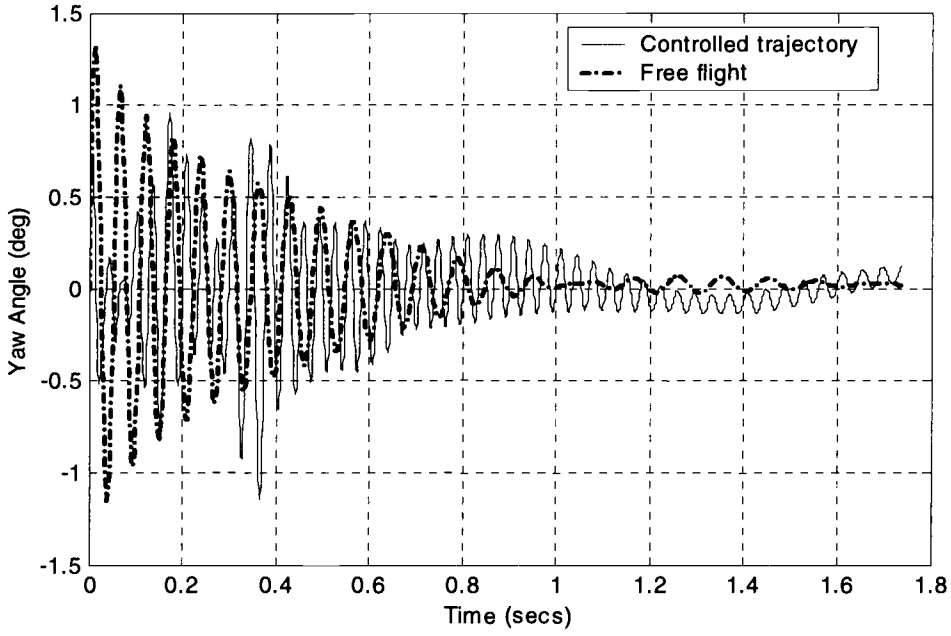

Figure 11. Yaw angle vs Time.

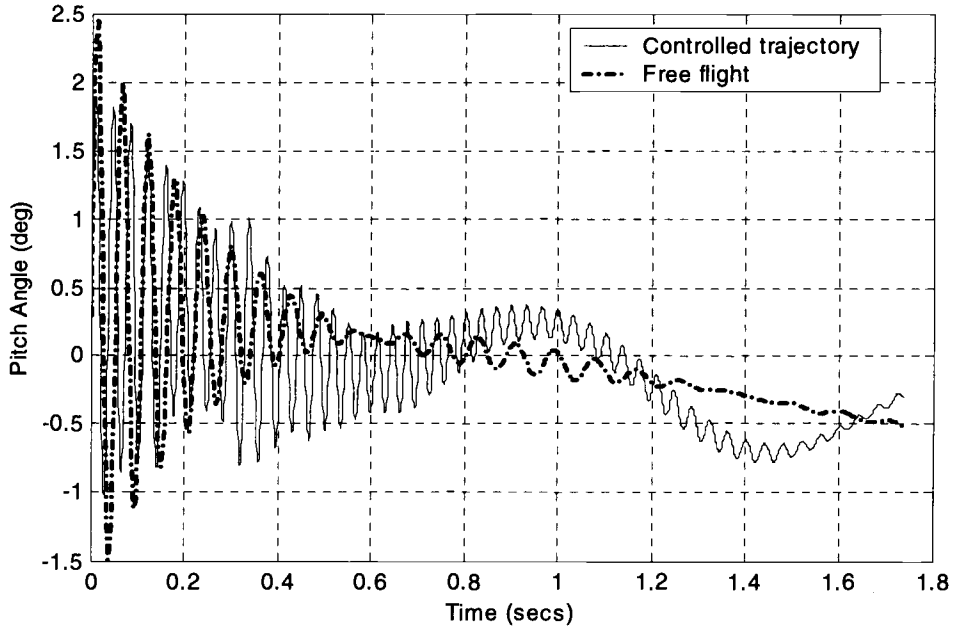

Figure 12. Pitch angle vs Time.

Figure 11 and 12 show the yaw and pitch angles for the controlled trajectory. The maximum value attained by the yaw and pitch angles is about 1 degree and 1.75 degrees respectively. In the transient phase of the response it is seen that the yaw and pitch angles for the controlled trajectory lag behind the uncontrolled trajectory. This can be attributed to the additional moments generated by the ram air mechanism which tend to smooth out the response.

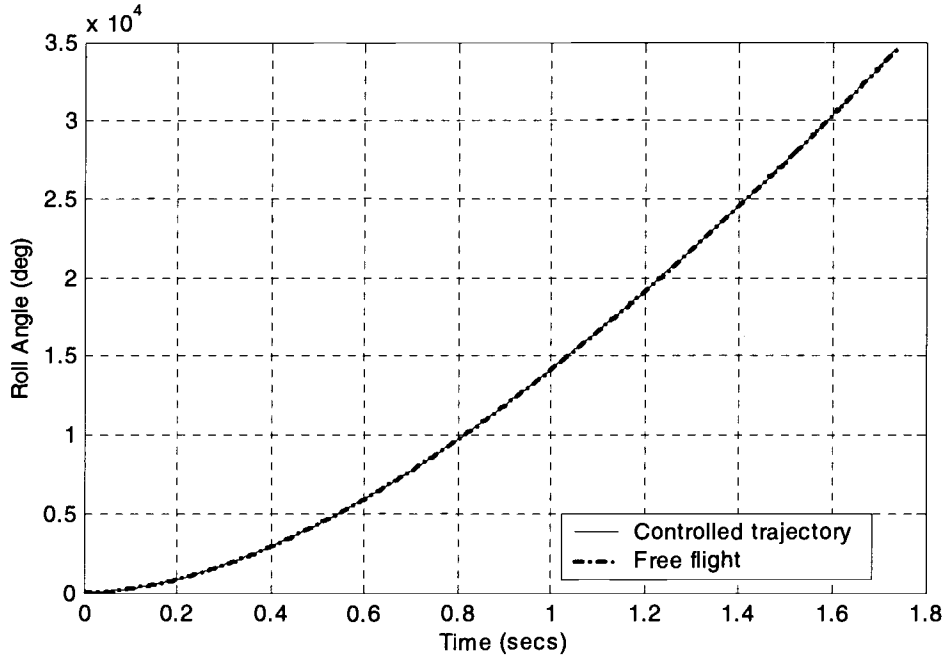

Figure 13. Roll angle vs Time.

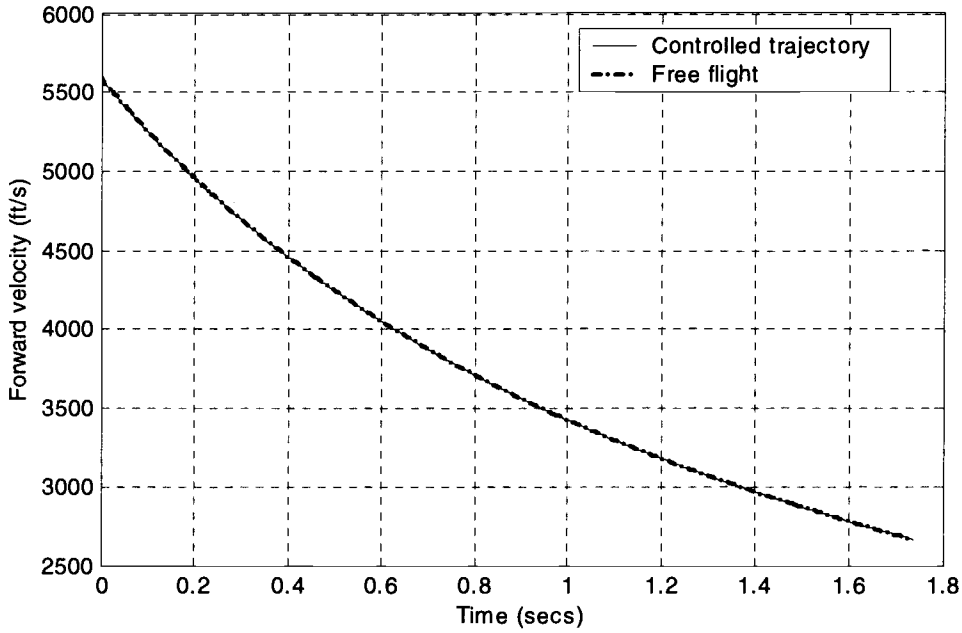

Figure 14. Forward velocity vs Time.

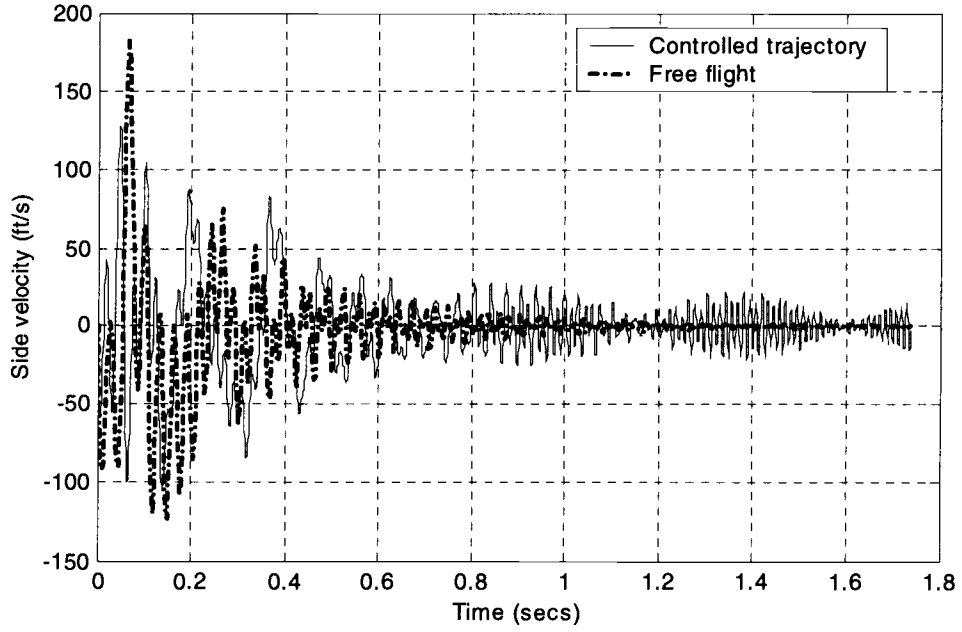

Figure 15. Side velocity vs Time.

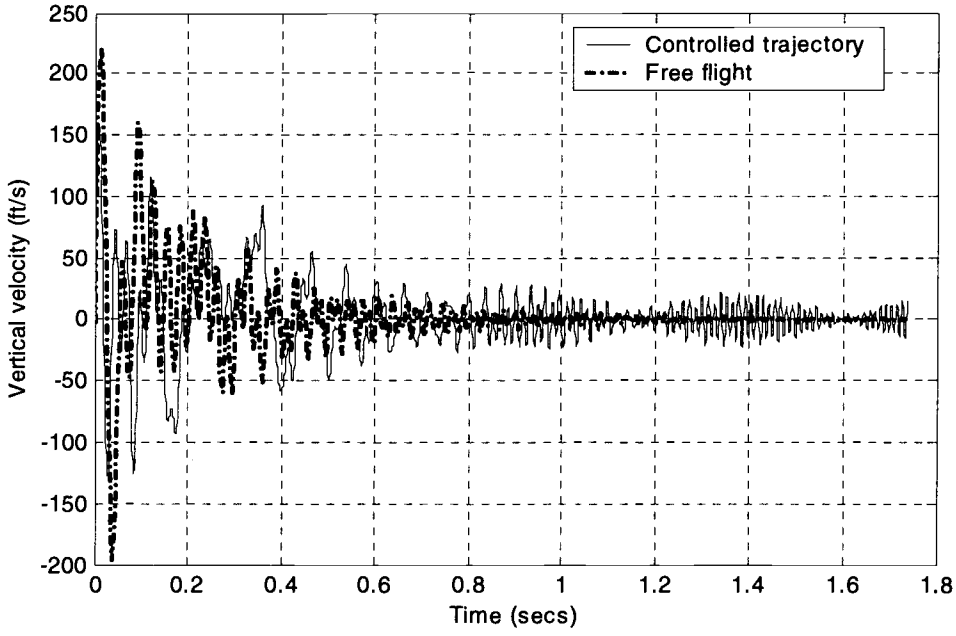

Figure 16. Vertical velocity vs Time.

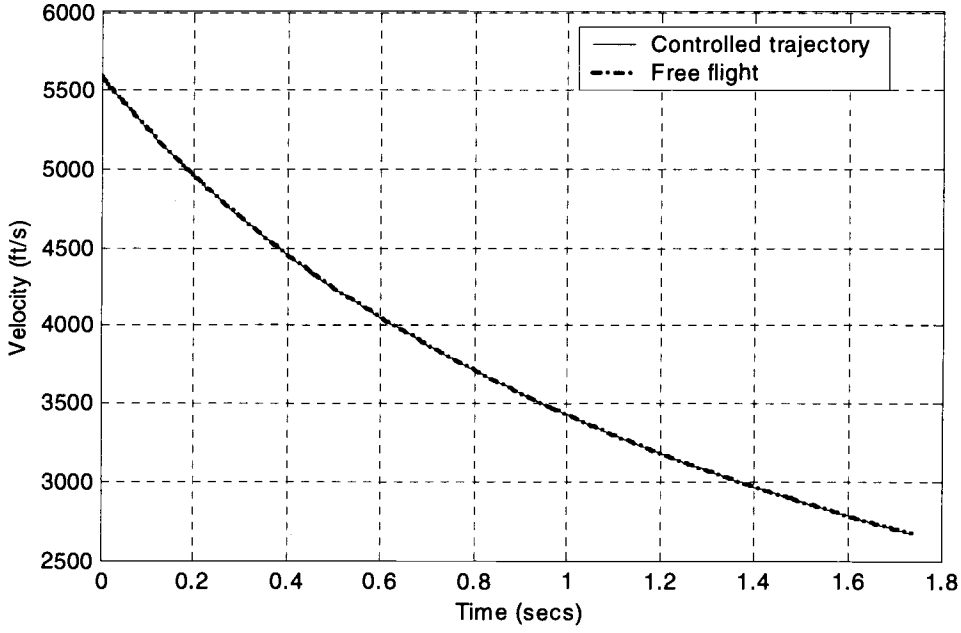

Figure 17. Total velocity vs Time.

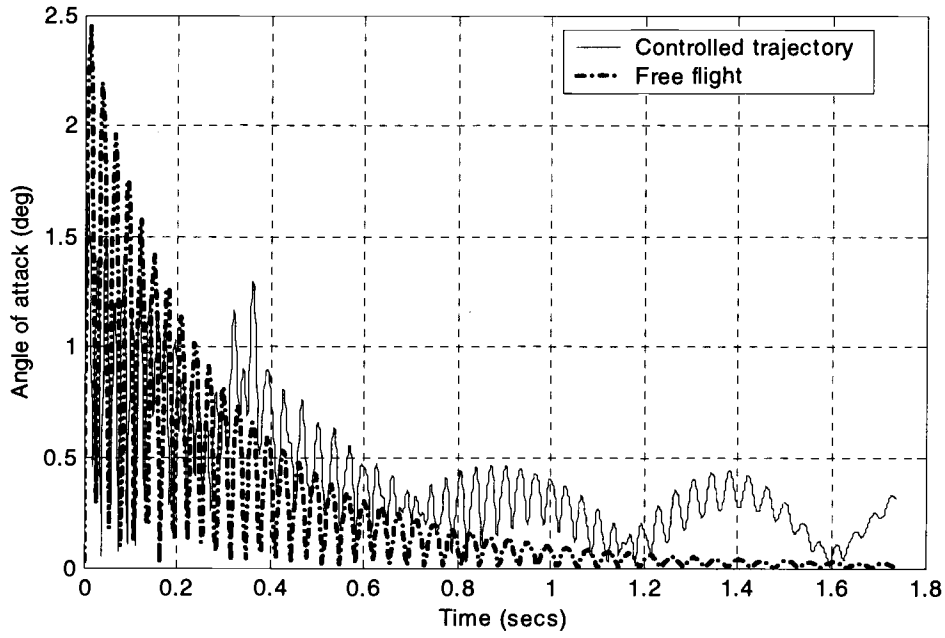

Figure 18. Angle of attack vs Time.

Figure 18 shows the variation of angle of attack with time. It is seen that the angle of attack variation is less than that for the uncontrolled flight in the transient phase of the response. The angle of attack attains a peak value of 1.5 degrees in the transient. This supports the assumption made during the ram air force calculation that the variation in angle of attack is small. This figure also establishes the stability of the internal dynamics.

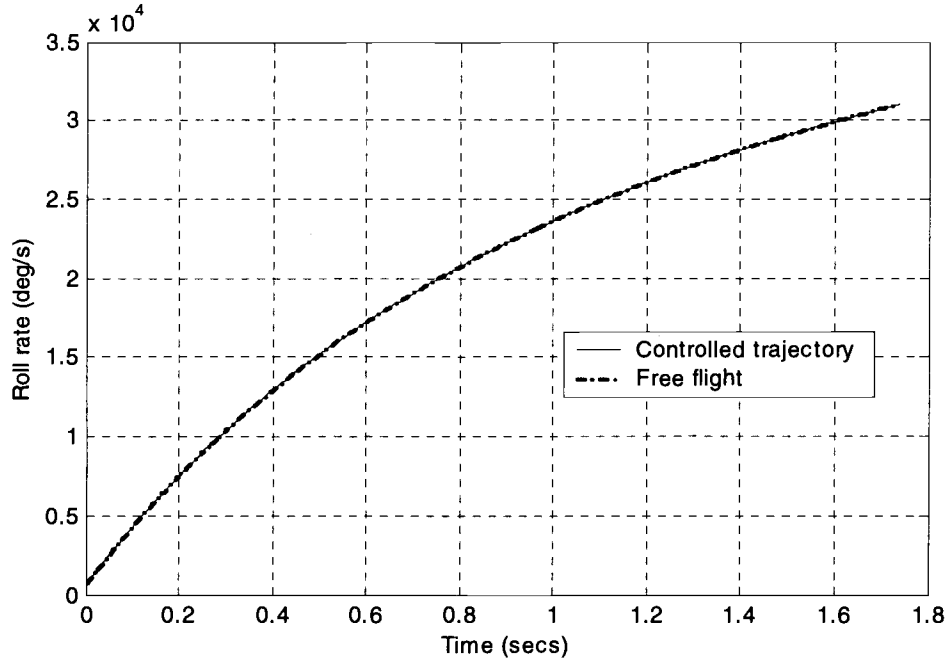

Figure 19. Roll rate vs Time.

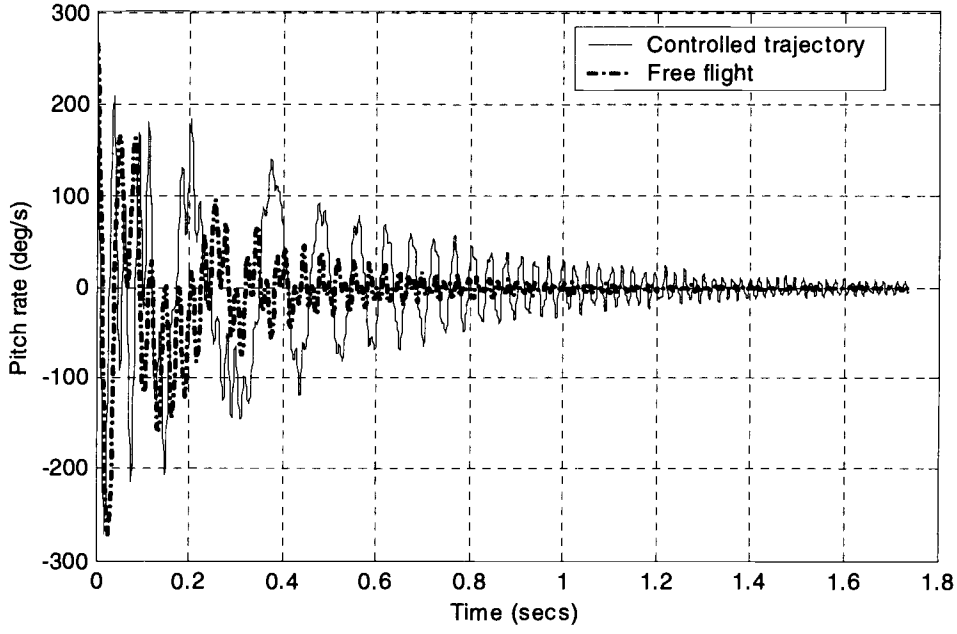

Figure 20. Pitch rate vs Time.

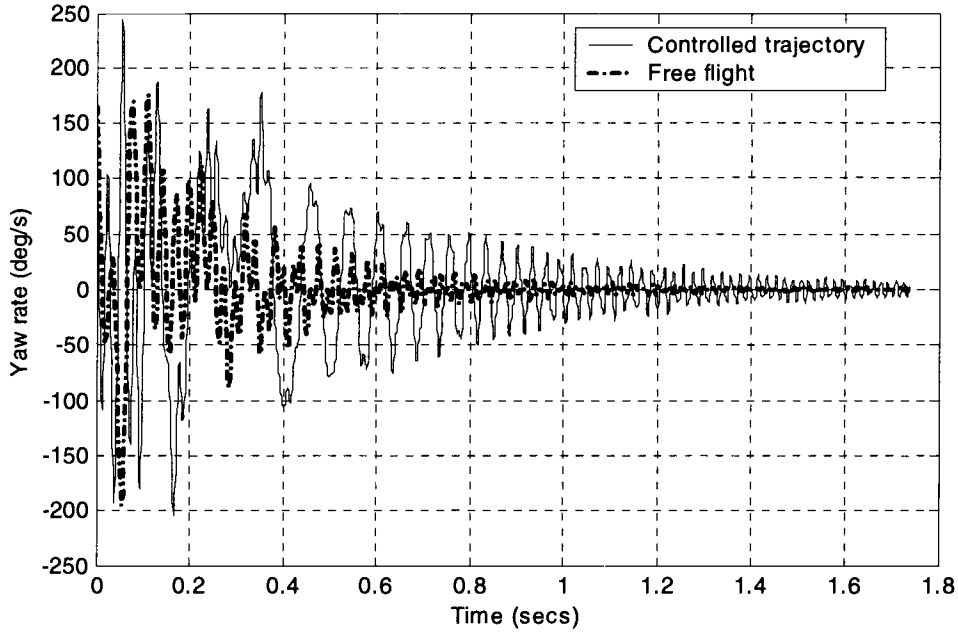

Figure 21. Yaw rate vs Time.

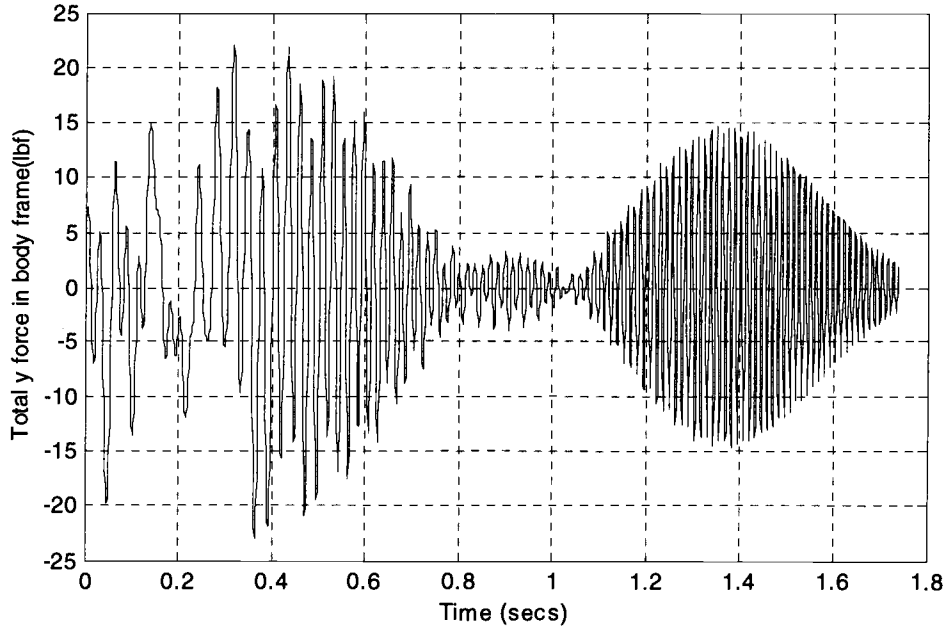

Figure 22. Commanded y force Y vs Time.

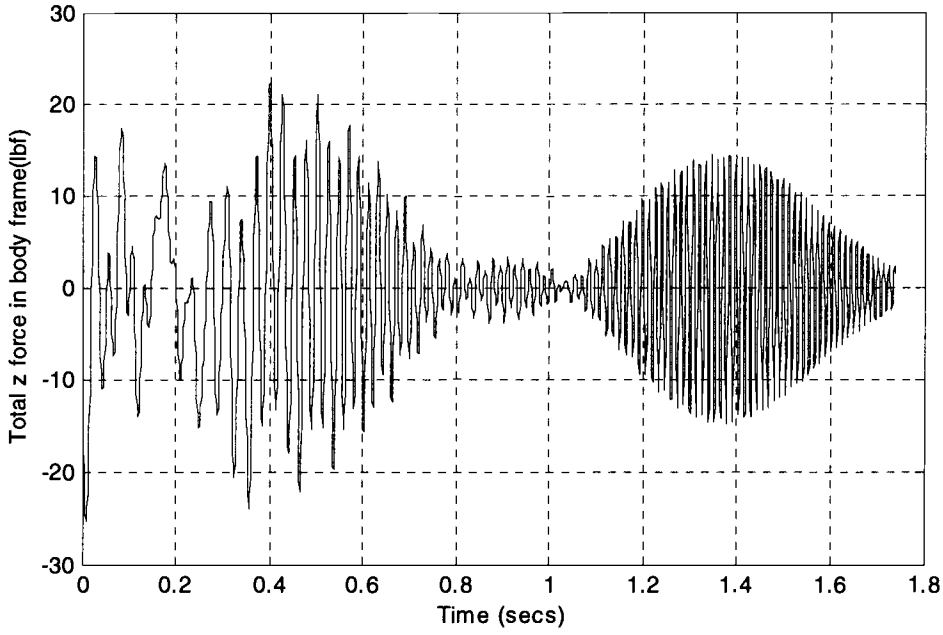

Figure 23. Commanded z force Z vs Time.

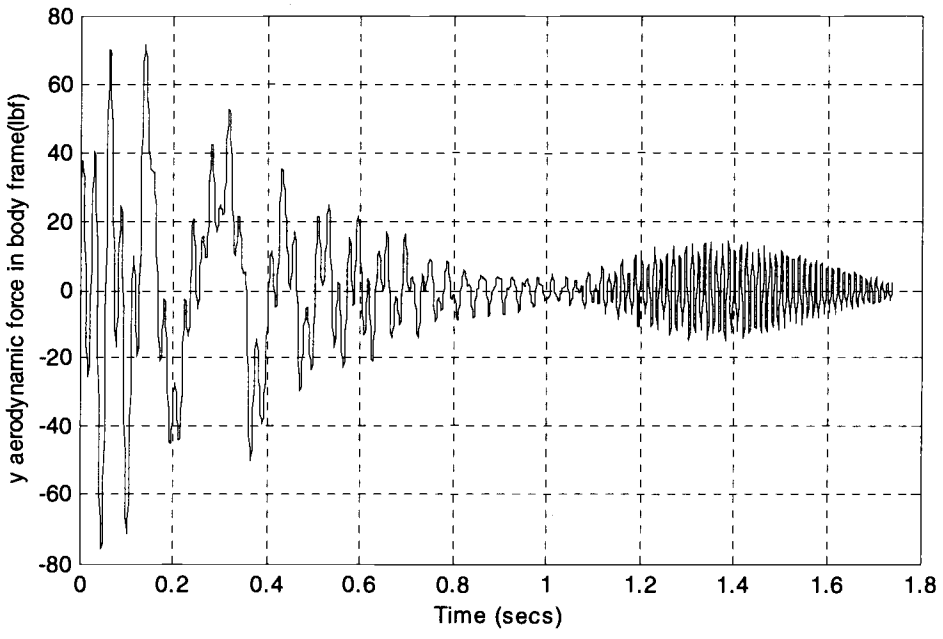

Figure 24. y aerodynamic force Y_A vs Time.

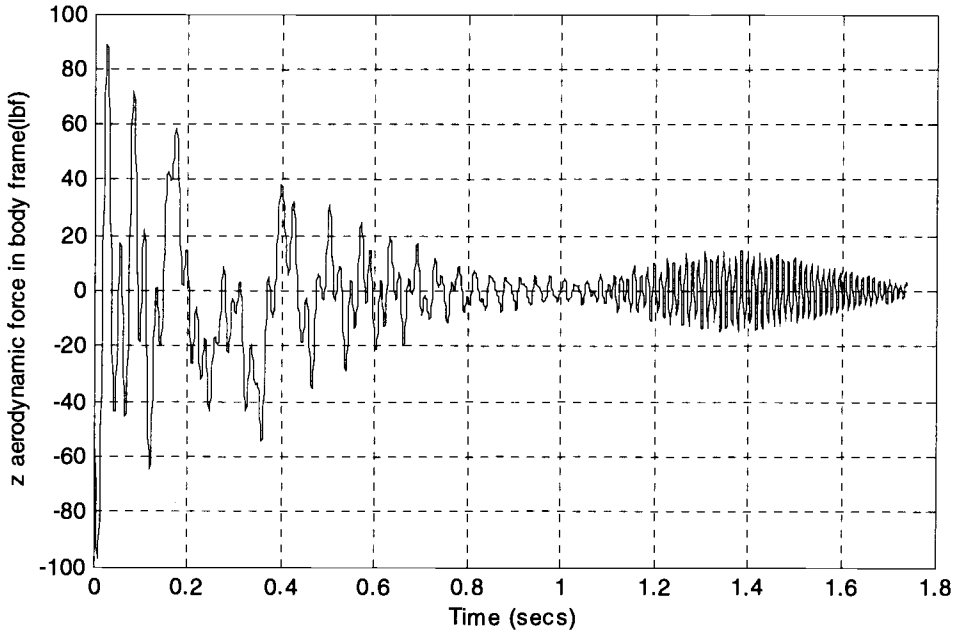

Figure 25. z aerodynamic force Z_A vs Time.

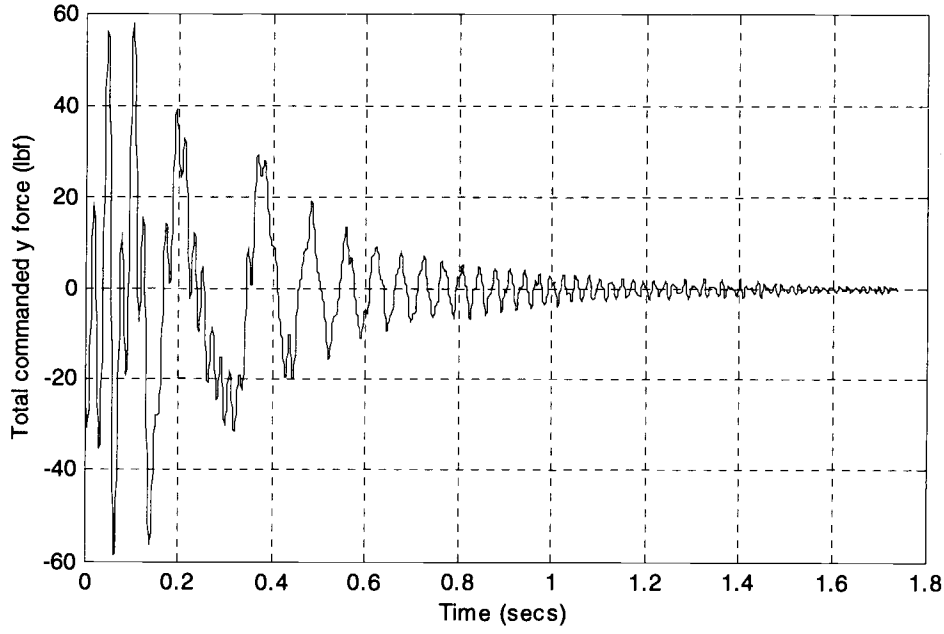

Figure 26. Total commanded y force vs Time.

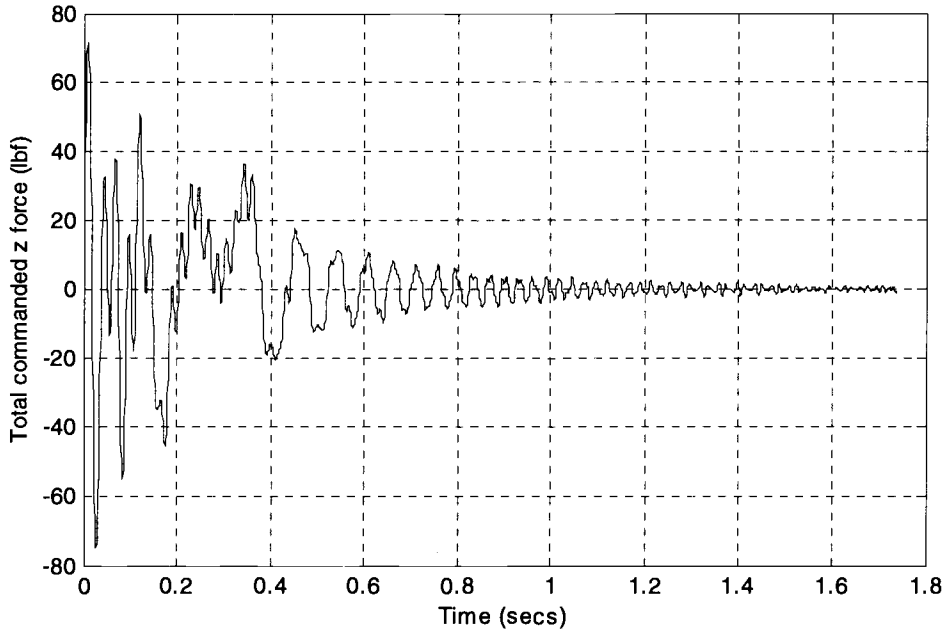

Figure 27. Total commanded z force vs Time.

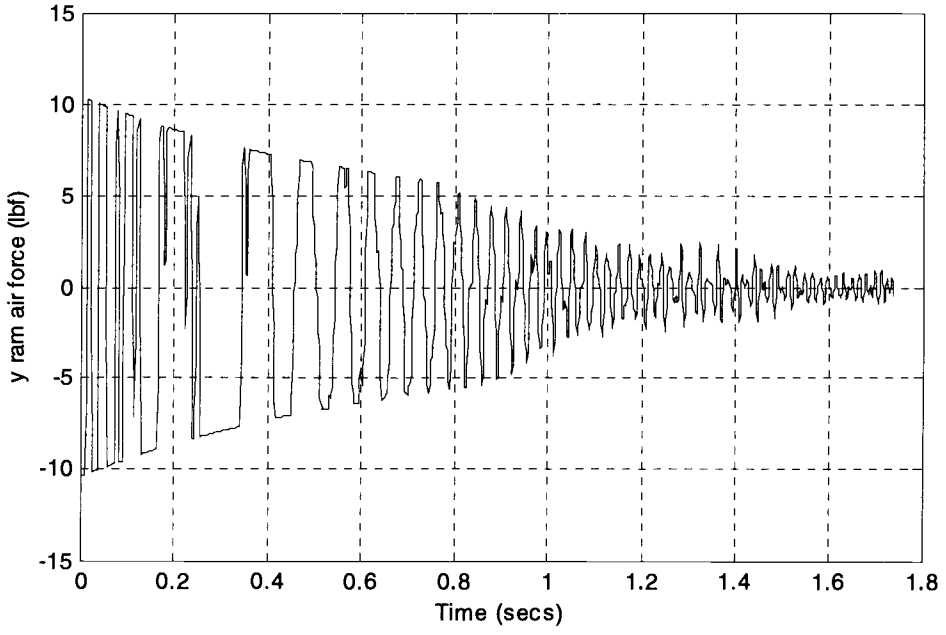

Figure 28. Actual y ram air force vs Time.

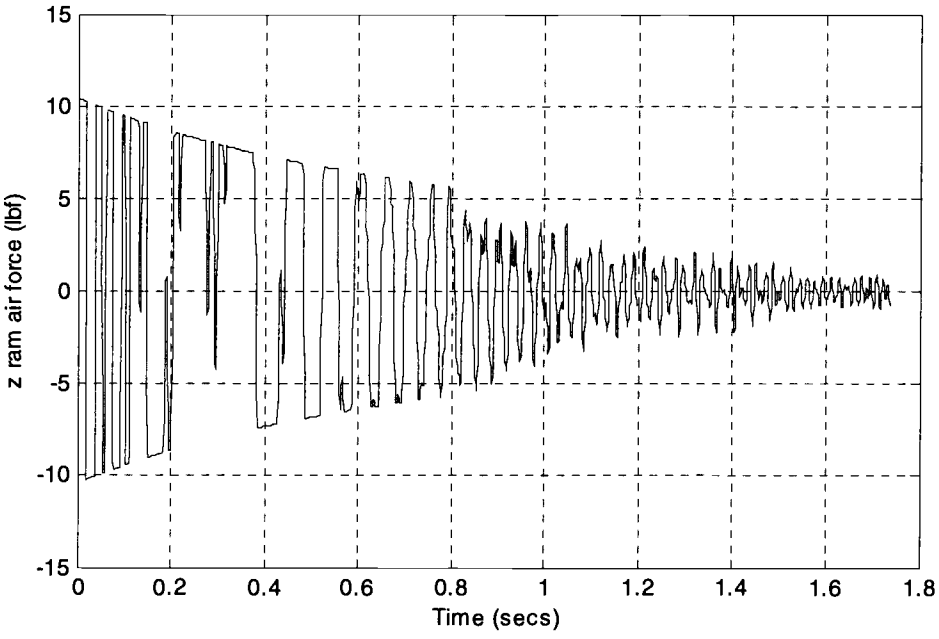

Figure 29. Actual z ram air force vs Time.

Figure 22 and 23 show the total force commanded in the body frame. This force represents the output of the linear controller transformed into the non-linear domain. Figure 24 and 25 show the aerodynamic force acting on the round. Figure 26 and 27 show the total force demanded from the ram air mechanism. Figure 28 and 29 show the actual force generated by the ram air mechanism.

In the initial phase of motion, the commanded forces act in a direction opposite to the standard aerodynamic forces so that when the aerodynamic forces are subtracted from the commanded forces to get the ram air forces, the magnitude of the resultant ram air force is greater than that of the commanded forces. Also, in the initial phase, the limit of the forces that can be produced by the ram air mechanism is exceeded as a result of which we see the actual force plot (Figure 28

and 29) being chopped off by a parabolic envelope which represents the limit of the lateral ram air forces. In the steady state, the forces are seen to stay well within the limits of the ram air mechanism.

Whenever the commanded ram air force exceeds the maximum limit, the corresponding sleeve valve is fully open. In the steady state, when the commanded ram air force is well below the maximum value, the sleeve valve is partially open. This model for the sleeve valve has not been included in this study.

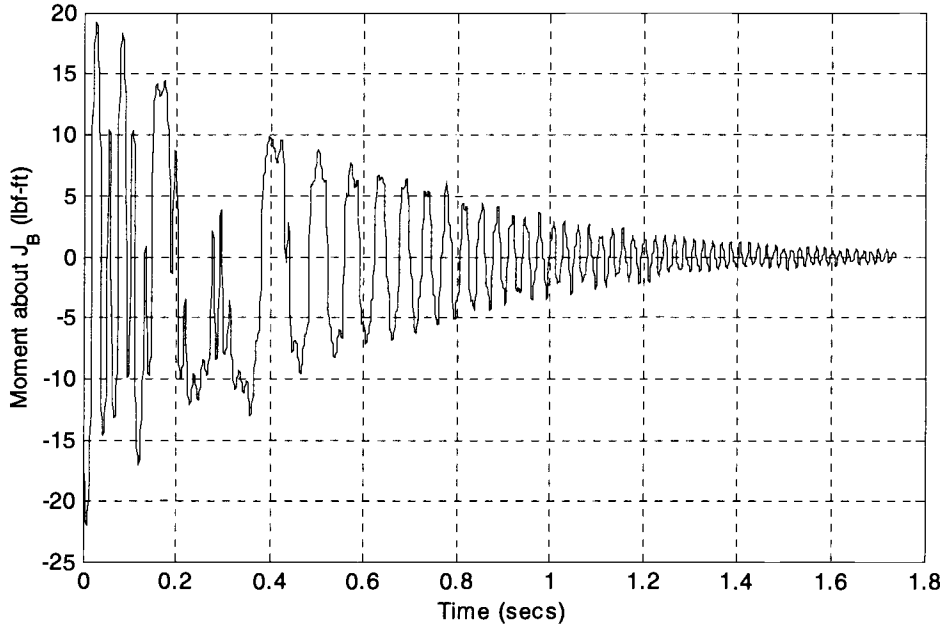

Figure 30. Moment M vs Time.

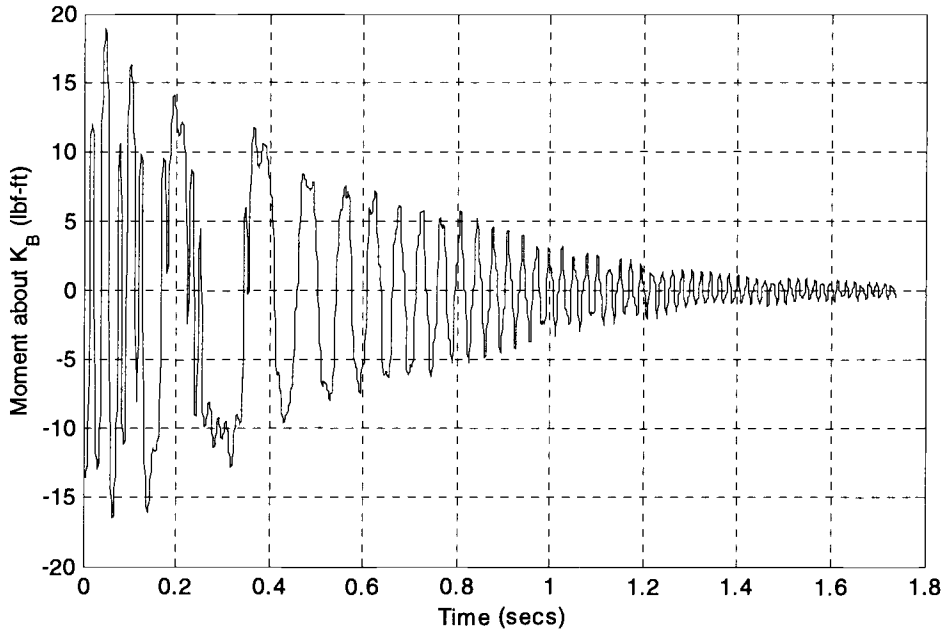

Figure 31. Moment N vs Time.

The results discussed so far pertain to a single perturbation. The results that follow pertain to Monte Carlo simulations for variations in different parameters.

Figure 32 shows the dispersion radius plot for perturbations in the yaw and the pitch rates. The initial yaw and pitch rates are perturbed 50 times with disturbances that have a mean of 0 rad/s and a standard deviation of 3 rad/s. If a plane parallel to the inertial yz plane is placed 2 kilometers downrange, a scatter of hit points represented by **x** is produced on the plane. If the hits points are arranged in ascending order of their distance from the mean hit point, the 34^{th} radius is called as the dispersion radius. In the case of free flight, i.e, uncontrolled flight, this value is seen to be 5.2222 ft. With the controller switched on, a scatter with individual hit points represented by **o** is obtained. The dispersion radius in this case is 0.1354 ft.

This represents a reduction of 39 times which demonstrates a vast improvement in the round performance.

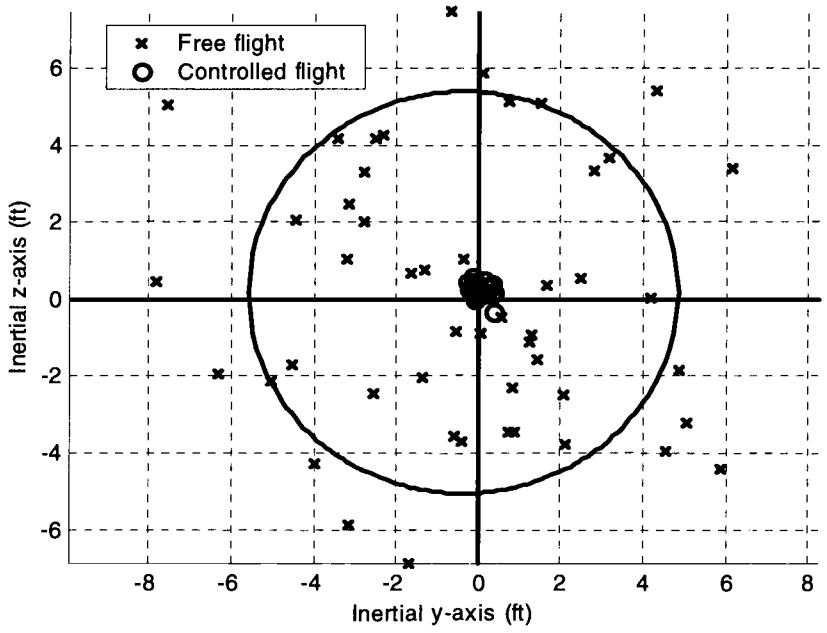

Figure 32. Dispersion plot for clean coordinates.

Figure 33 shows the variation of dispersion radius with maximum sleeve valve diameter also termed as orifice diameter. Set 1, set 2 and set 3 are three sets of fifty perturbations each in the yaw and pitch rates. The mean value for all of them is 0 rad/s. The standard deviation for set 1, set 2 and set 3 is 3 rad/s, 5 rad/s and 7 rad/s respectively. With increase in diameter, the maximum force available at each Mach number considered increases as a result of which the dispersion radius is seen to decrease with increasing orifice diameter for each of the perturbation sets. At higher diameter values the curves even out becoming almost parallel to the

abscissa. Increase in the standard deviation of perturbation rates is seen to move the curves towards greater values of dispersion radius.

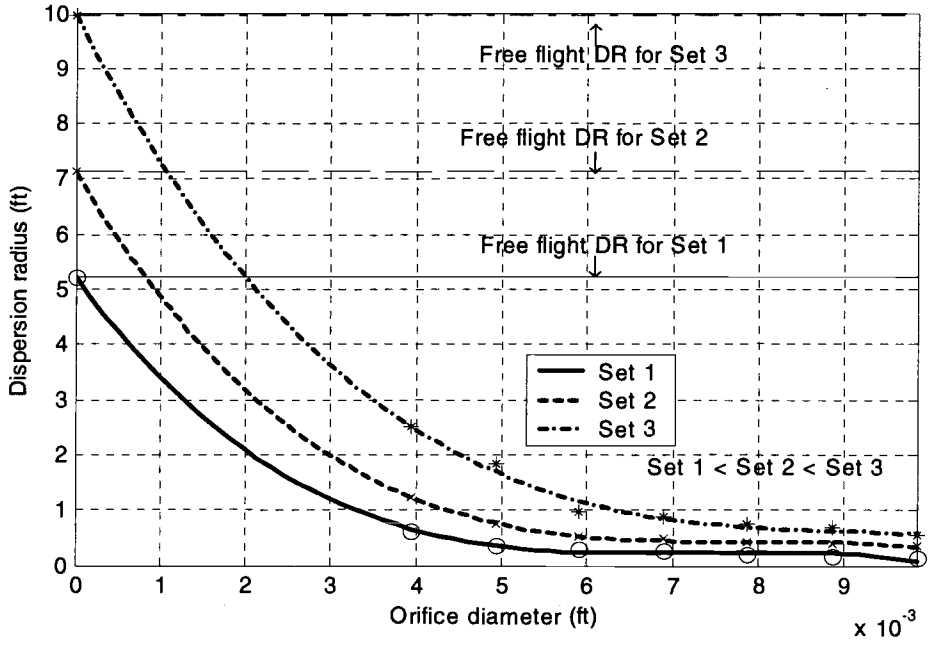

Figure 33. Effect of initial value perturbations on Dispersion.

Figure 34 evaluates the effect of IMU noise and bias on the performance of the round. The accelerometer and gyroscope noise and bias are subjected to 6 sets of perturbations. The mean value of the perturbations is zero. Table 4 lists the standard deviation for each of these sets.

The curves move towards increasing values of dispersion radius with increase in standard deviation of noise and bias. The curves associated with sets 1 to 4 lie below the free flight curve, which is essentially a straight line. For these sets the dispersion radius decreases with increase in orifice diameter. The curves

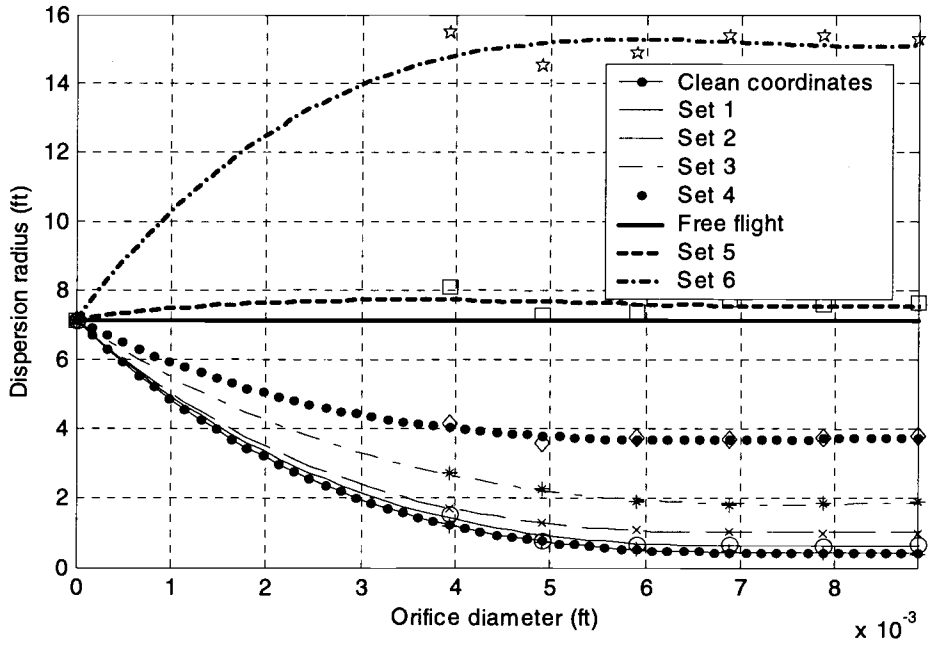

Figure 34. Effect of noise and bias on Dispersion.

	Gyrometers		Accelerometers	
	Bias (rad/s)	**Noise (rad/s)**	**Bias (ft/s^2)**	**Noise (ft/s^2)**
Set 1	0.000875	0.001750	0.161000	0.032200
Set 2	0.001750	0.003500	0.322000	0.064400
Set 3	0.003500	0.007000	0.644000	0.128800
Set 4	0.007000	0.014000	1.288000	0.257600
Set 5	0.014000	0.028000	2.576000	0.515200
Set 6	0.028000	0.056000	5.152000	1.030400

Table 4. Standard deviations for IMU perturbations.

associated with sets 5 and 6 lie above the free flight curve. Curve 5 is almost parallel to the abscissa. Curve 6 shows an interesting behaviour. At lower values of orifice diameter for this curve, the dispersion radius is less than that at higher

values. At higher values of IMU bias and noise, the dispersion radius for the falsified trajectories is larger. The controller tries to track these trajectories. But the quality of tracking depends on the force available from the ram air mechanism. At higher values of IMU noise and bias, higher force will be needed. But with lower diameter values, this cannot be generated and so the round ends up closer to the (0,0) point thus making the dispersion radius smaller for lower values of orifice diameter.

7. CONCLUSIONS AND RECOMMENDATIONS

7.1 CONCLUSIONS

The dynamic simulation shows the performance of a smart penetrator round with an actively controlled ram air mechanism. As seen from the dispersion plots, the improvement in performance is significant, i.e, the dispersion reduces by 39 times. This proves that the ram air mechanism is an effective and viable control mechanism for small and medium sized rounds with high initial velocity. The control force generated by the ram air mechanism is sufficiently high at higher round velocities.

Noise and bias have an adverse effect on the performance of the controller. Random perturbations in the noise and bias are seen to increase the dispersion indicating that noise and bias in both the accelerometer and bias must be eliminated. If these cannot be fully eliminated they must be at least limited to the lowest possible values. It is seen that the controller can tolerate moderate amount of noise and bias when the dispersion radius is less than the free flight dispersion.

7.2 RECOMMENDATIONS

In this study, a very simple model is developed for the ram air forces. It is assumed that a normal shock exists at the inlet with an attached shock around the conical nose of the projectile. The ram air forces are calculated with these

assumptions. A more detailed force analysis utilizing numerical methods can provide a better insight into the actual flow field. Even better would be the experimental estimation of the aerodynamic forces. Ram air cavities could be made in the nose of the round and the round fired in ballistic ranges. Another way would be to use a wind tunnel for the above said purpose.

Noise and bias in the IMU are seen to be the major cause for deterioration in controller performance. The IMU is essential as the flight controller needs estimates of the local coordinates. An observer is one way to circumvent this problem. If the IMU is replaced with a non-linear observer then the effects of noise and bias can be totally eliminated.

REFERENCES

[1] C.O. White, N.G. Hempling, R.J. Prodan, L.W. Conboy, "Automatic Cannon Caliber Maneuvering Projectile: Design Concept Study", Ford Aerospace and Communications Corporation, Newport Beach, CA, Final Technical Report, ARRADCOM Support Activity, Picatinny Arsenal, NJ, 1982.

[2] R. Gast, S. Morris, M. Costello, "Simulation of Shot Impacts for the M1A1 Tank Gun," Journal of Guidance, Control, and Dynamics, Volume 23, Number 1, pp. 53-59, 2000.

[3] Jean-Jacques E. Slottine, Weiping Li, "Applied Nonlinear Control", Prentice Hall, Englewood Cliffs, New Jersey 07632, 1991.

[4] Alberto Isidori, "Nonlinear Control Systems", Springer, 3rd edition, 1995.

[5] Robert L. McCoy, "Modern Exterior Ballistics The Launch and Flight Dynamics of Symmetric Projectiles", Schiffer Military History, 1999.

[6] L.R. Hunt, Renjeng Su, G. Meyer, "Design for multi-input nonlinear systems", Proceedings of conference held at Michigan Technological University, June 28 – July 2, 1982.

[7] James J. Romano, Sahjendra N. Singh, "Inversion of Nonlinear I-O Map, Zero Dynamics and Flight Control System Design", AIAA GNC, Aug 20-22, 1990, Portland, Oregon, Vol I of II.

[8] S. Antony Snell, Dale F. Enns, William L. Garrard Jr., "Nonlinear Inversion Flight Control for a Supermaneuverable Aircraft", AIAA GNC, Aug 20-22, 1990, Portland, Oregon, Vol I.

[9] Robert F. Antoniewicz, Eugene L. Duke , P.K.A. Menon, "Flight Test of a Trajectory Controller using Linearising Transformations with measurement feedback", AIAA GNC, Aug 20-22, 1990, Portland, Oregon, Vol I.

[10] Donald E. Beasley, Richard S. Figliola, "Theory and Design of Mechanical Measurements", John Wiley & Sons, 3rd edition, 2000.

[11] Bernard Etkin, "Dynamics of Atmospheric Flight", John Wiley and Sons, New York, 1972.

[12] Robert D. Zucker, "Fundamentals of Gas Dynamics", Matrix Publishers, 1977.

[13] John J. Bertin, Michael L. Smith, "Aerodynamics for Engineers", Prentice Hall, 3rd edition, 1998.

[14] Shmuel Merhav, "Aerospace Sensor Systems and Applications", Springer, 1996.